Mechanisms leading to exceptional niobium concentration during lateritic weathering: The key role of secondary oxides

Quentin Bollaert, Mathieu Chassé, Artur Bastos Neto, Benoît Baptiste, Alexandra Courtin, Laurence Galoisy, Olivier Mathon, Cécile Quantin, Delphine Vantelon, Georges Calas

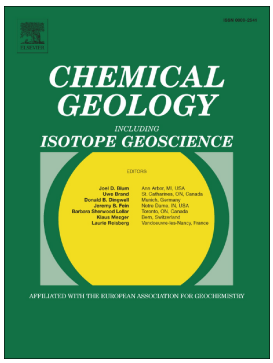

Mechanisms leading to exceptional niobium concentration during lateritic weathering: The key role of secondary oxides

Quentin Bollaert, Mathieu Chassé, Artur Bastos Neto, Benoît Baptiste, Alexandra Courtin, Laurence Galoisy, Olivier Mathon, Cécile Quantin, Delphine Vantelon, Georges Calas

PII: S0009-2541(23)00468-0

DOI: https://doi.org/10.1016/j.chemgeo.2023.121767

Reference: CHEMGE 121767

To appear in: *Chemical Geology*

Received date: 26 June 2023

Revised date: 2 October 2023

Accepted date: 4 October 2023

Please cite this article as: Q. Bollaert, M. Chassé, A.B. Neto, et al., Mechanisms leading to exceptional niobium concentration during lateritic weathering: The key role of secondary oxides, *Chemical Geology* (2023), https://doi.org/10.1016/j.chemgeo.2023.121767

Mechanisms leading to exceptional niobium concentration during lateritic weathering: the key role of secondary oxides

Authors: Quentin Bollaert[1,*], Mathieu Chassé[1], Artur Bastos Neto [2], Benoît Baptiste[1], Alexandra Courtin[3], Laurence Galoisy[1], Olivier Mathon[4], Cécile Quantin[3], Delphine Vantelon[5], Georges Calas[1]

Affiliations:

[1]Sorbonne Université, Institut de Minéralogie, de Physique des Matériaux et de Cosmochimie, 4 place Jussieu, Paris, 75005, France

[2]Instituto de Geociências, Universidade Federal do Rio Grande do Sul, Avenida Bento Gonçalves 950, CEP 91540–970, Porto Alegre, RS, Brazil

[3]Université Paris-Saclay, UMR 8148 GEOPS, 91405 Orsay Cedex, France

[4]European Synchrotron Radiation Facility, 71, Avenue des Martyrs, 38000 Grenoble, France

[5]Synchrotron SOLEIL, L'Orme des Merisiers, Saint-Aubin, BP 48 91192 Gif-sur-Yvette Cedex, France

*corresponding author : quentin.bollaert@sorbonne-universite.fr

ABSTRACT

Niobium (Nb) is considered as one of the most immobile elements during supergene weathering due to its low solubility and the expected resistance of the pyrochlore mineral group ($A_2B_2X_6Y$) in which Nb occupies the B site. Although the resistance of pyrochlore is challenged by direct evidence of alteration in lateritic profiles, the geochemical and mineralogical processes controlling its behavior in the critical zone remains elusive, This study uses a multiscale geochemical, mineralogical and spectroscopic approach to monitor Nb solid speciation in a thick weathering profile. The weathering of the pyrochlore-bearing core carbonatite facies from Morro dos Seis Lagos has resulted in a Fe-enriched laterite with exceptional Nb concentrations (2.91 wt% Nb_2O_5 on average). The preservation of the successive secondary phases (Ti-, Fe-, Ce-oxides) resulting from weathering processes along the horizons offers the opportunity to track Nb during pyrochlore alteration from the fresh parent rock to the final stages of weathering. Intense lateritization processes have lead to an enrichment in Fe and Ti in the pyrochlore B-sites, resulting in the weakening of the structure and its ultimate destabilization due to weaker B–O bonds. After the release of Nb from pyrochlore, the fate of Nb is dependent on the secondary phases formed during weathering. In the lower horizons dominated by Fe oxides, goethite is the main host for Nb (1 wt% Nb_2O_5) due to its capacity to substitute Fe^{3+} for Nb^{5+}, in contrast to hematite. In the upper horizons, where Ti oxides have formed during the reworking of the laterite, Nb^{5+} is preferentially incorporated into brookite and rutile (20 wt% Nb_2O_5), which may have formed owing to slightly acidic pH and high Nb activity during their growth. The presence of Nb in hollandite and cerianite in a vein from the manganiferous horizon involves the transport of Nb with mobile elements at the scale of the laterite. With this study, we describe a new model accounting for the formation of Nb-enriched laterites. The latter is based on the ability of Nb^{5+} to substitute for Fe^{3+}, Ti^{4+}, Ce^{4+} in minerals formed by lateritization processes after its release from pyrochlore. The nature of the secondary Nb-bearing oxides is dependent on the chemistry of the parent rock and the conditions of

formation of the laterite. This work, evidencing the mobilization of Nb both at the scale of the mineralogical assemblage and of the entire profile questions the pervasive use of Nb as a geochemical invariant in the critical zone.

KEYWORDS: NIOBIUM, LATERITE, WEATHERING, SPECIATION, X-RAY ABSORPTION SPECTROSCOPY, PYROCHLORE

1. INTRODUCTION

Niobium (Nb) is used as a chemical invariant to trace geological processes, in particular, supergene weathering due to its expected immobility resulting from the resistance to alteration of Nb-bearing minerals and its low solubility in fluids (Nahon and Merino, 1996; Kurtz et al., 2000; Peiffert et al., 2010, Guinoiseau et al., 2021). As Nb is a technology-critical element, our understanding of the geochemical behavior of Nb in the critical zone results from studies on highly-weathered regoliths in which Nb reaches economic levels (Cordeiro et al., 2011; Braga and Biondi, 2023). Intense weathering of Nb-enriched carbonatites hosting pyrochlore-supergroup minerals ($A_{2-x}B_x(O,OH)_6(OH,F,H_2O)_{1-y}$) leads to Nb enrichment relative to the primary carbonatite (Mitchell, 2015). The A-site of pyrochlore can be occupied by several cations including Na^+, Ca^{2+}, Mn^{2+}, Sr^{2+}, Ba^{2+}, Pb^{2+} or rare-earth elements (REE^{3+}). The B-site is occupied by sixfold-coordinated cations such as Nb^{5+}, Ta^{5+}, Ti^{4+}, Fe^{3+}, Al^{3+}, Si^{4+} (Atencio, 2021). The formation of such Nb-enriched weathering covers is expected to result from the resistance of pyrochlore to alteration which leads to its physical accumulation in the profile while carbonates are dissolved (Williams et al., 1997; Nasraoui and Billal, 2000; Cordeiro et al., 2011; Mitchell, 2015; Williams-Jones and Vasyukova, 2022). The alteration of pyrochlore leads to ion-exchanges occurring at the A- and Y-sites (Lottermoser and England, 1988; Wall et al., 1996; Cordeiro et al., 2011) and to the formation of vacancies (Lumpkin et al., 2000; Geisler et al., 2004). Altered pyrochlore in laterites are characterized by higher concentrations of Ba, Ce and Sr which have replaced Ca and Na at the A-

sites as is the case in the Araxá and Catalão-I world-class Nb deposits (Rocha et al., 2001; Cordeiro et al..2011, Palmieri et al., 2022; Braga and Biondi, 2023). In these laterites, the stability of pyrochlore during alteration is thought to be preserved by the strongly-bonded B_2X_6 octahedral framework which maintains its structure (Lumpkin et al.,, 2000).

However, evidence of pyrochlore alteration in several laterites worldwide questions the immobility of Nb in supergene context. In the laterite formed from the weathering ofthe Mount Weld carbonatite, Nb is found in mineral phases in the vicinity of pyrochlore such as Fe oxides, anatase and crandallite resulting from the alteration of primary phases (Lottermoser and England, 1988). Hydropyrochlore from the Lueshe laterite (formerly known as kalipyrochlore) is also replaced by Nb-bearing crandallite and goethite (Wall et al., 1996). Finally, Nb-bearing goethite has been identified in regoliths formed by the weathering of Chuktukon and Tchivira pyrochlore-bearing carbonatites (Melgarejo et al., 2012; Chebotarev et al., 2017). Nevertheless, the processes leading to the complete alteration of pyrochlore, the scavenging of Nb in secondary oxides and their contribution to the average Nb speciation relative to pyrochlore at the laterite scale have never been studied.

The Morro dos Seis Lagos lateritic cover (Amazonas, Brazil) constitutes a unique opportunity to explore the processes of pyrochlore alteration through supergene processes. This thick profile (> 100 m), formed over a siderite ($FeCO_3$) carbonatite (0.8–1.0 wt % Nb_2O_5) exhibits exceptional Nb concentrations (2.91 wt % Nb_2O_5 in average, Giovannini et al., 2017). The weathering processes have lead to a significant enrichment in Nb by a factor three to four relative the grade of the fresh carbonatite. Such enrichment factor is higher than that of the Araxá and Catalão-I world-class Nb deposits, where the enrichment factor is typically one to two (Chakhmouradian et al., 2015). The primary Nb hosts in carbonatite have been described as Ce-Ba-bearing pyrochlore and Nb-bearing brookite (Giovannini et al., 2020). Niobium mineralization in the lateritic profile is unusual as pyrochlore is not found in the horizons above the brown laterite (above 58 m in depth), suggesting

an efficient dissolution during the lateritization processes (Giovannini et al., 2017; Williams-Jones and Vasyukova, 2022). Instead, Nb is identified in rutile (11–27 wt% Nb_2O_5), brookite (10–16 wt% Nb_2O_5), goethite (up to 3 wt % Nb_2O_5) and cerianite (up to 0.75 wt % Nb_2O_5) although their conditions of formation and contribution to the average Nb speciation remain unknown (Giovannini et al., 2017, 2021).

In this study, we use a multiscale approach combining bulk techniques (inductively coupled plasma mass spectrometry – ICP-MS – and synchrotron high-resolution X-ray diffraction – HR-XRD), micrometric-scale observations (electron probe microanalysis – EPMA – and scanning electron microscopy – SEM) and atomic-scale analyses (X-ray absorption near-edge structure – XANES – and extended absorption fine structure – EXAFS – spectroscopies) in order to quantitatively monitor the average Nb speciation along a weathering profile from Morro dos Seis Lagos lateritic cover (Giovannini et al., 2017). Applying this approach on the successive weathering phases along the horizons offers the opportunity to follow Nb behavior during pyrochlore alteration up to the final stages of alteration.

2.1 Geological context and samples

The Morro dos Seis Lagos complex consists of three circular bodies elevated at 300–400 m height located in the southwestern part of the Guiana Shield (Issler and Silva, 1980). The main carbonatite body is about 3 km in diameter (Fig. 1). The age of the emplacement of the carbonatite is uncertain. U-Pb dating on zircon yields a maximum age of 1.3 Ga, suggesting an evolution related to the genesis of the K'Mudku belt (Rossoni et al., 2017). Isotopic data suggest a younger age of 200 Ma whose formation is associated with the Taiano and Penatecaua magmatism (Giovannini et al. 2020). The extensive dissolution of carbonates in the presence of waters equilibrated with atmospheric CO_2 combined with a humid tropical climate since at least the Eocene (Vasconcelos et al., 1994) have led to the formation of a thick lateritic cover reaching a thickness of

more than 250 m in places (Giovannini et al., 2017).

Here, we study the SG-01-AM drill hole of 100 m depth collected by the Companhia de Perquisa de Recursos Minerais (CPRM) (Viegas Filho and Bonow, 1976). This profile has been divided by Giovannini et al., (2017) into six textural and compositional types from the top to the bottom (Fig. 2a): (1) pisolitic laterite, (2) fragmented laterite, (3) mottled laterite, (4) purple laterite, (5) manganiferous laterite, (6) brown laterite (Giovannini et al., 2017). The top three horizons result from physical and chemical reworking near the surface (Fig. 2a). Of note, the manganiferous horizon consists in a ferruginous horizon crosscut by centimetric veins or irregular masses of Mn oxides. The other part of the profile from 100 m down to 250 m depth which comprises the underlying siderite carbonatite could not be collected (Giovannini et al., 2020). The carbonatite parent rock presented in this study is the 'core carbonatite' described in Giovannini et al., (2017), which has been collected in SG-04-AM drill hole between 280 and 343 m depth. The core carbonatite has been sampled one kilometer east from the studied profile (Fig. 1b).

2.2 Bulk mineralogical and geochemical characterization

Synchrotron high-resolution XRD (HR-XRD) was performed on ca. 20 mg of powder in 0.3 mm borosilicate capillaries on the two-circle diffractometer of the CRISTAL beamline of SOLEIL synchrotron. The diffraction measurements were performed in transmission geometry using a Mythen2 X 9K detector (Dectris®) at $\lambda = 0.58187$ Å (5 min acquisition time). Representativeness of the bulk powder was tested by comparing the intensity of the main diffraction peaks resulting from the analysis of 3 g of powder using conventional XRD. Major phases were identified using the PDF4+ Minerals Database by the International Center for Diffraction Data (ICDD). Quantitative evolution of the mineral proportions was assessed by the Rietveld method using the FullProf suite (Rodríguez-Carvajal, 1993). The scale factors, unit-cell parameters, isotropic Debye-Waller factors and Lorentzian isotropic shape of the peaks (Y) of each phase were refined in order to fit the theoretical patterns calculated from the crystal structures with the

experimental one. The error on the proportion of the phases given by FullProf is about 1 % f or Fe oxides and < 0.5 % for the other phases.

Whole rock geochemical analyses were performed by ACME Analytical Laboratories Ltd (Canada) and come from Giovannini et al., (2017). Major oxides (SiO_2, Al_2O_3, Fe_2O_3, MgO, CaO, Na_2O, K_2O, TiO_2, P_2O5, MnO, Cr_2O_3) and trace elements (Ba, Be, Co, Cs, Ga, Hf, Nb, Ni, Rb, Sc, Sn, Sr, Ta, Th, U, V, W, Zr, plus REE) were analyzed by ICP-MS after alkaline fusion and nitric acid digestion of 0.2 g aliquots. Another set of trace elements (Ag, As, Au, Bi, Cd, Cu, Hg, Mo, Ni, Pb, Sb, Se, Tl, Zn) was analyzed by ICP- MS after aqua regia digestion of 0.5 g aliquots. Loss on ignition was obtained by weight difference after ignition at 1000 °C. A Leco furnace was used to measure total C and S.

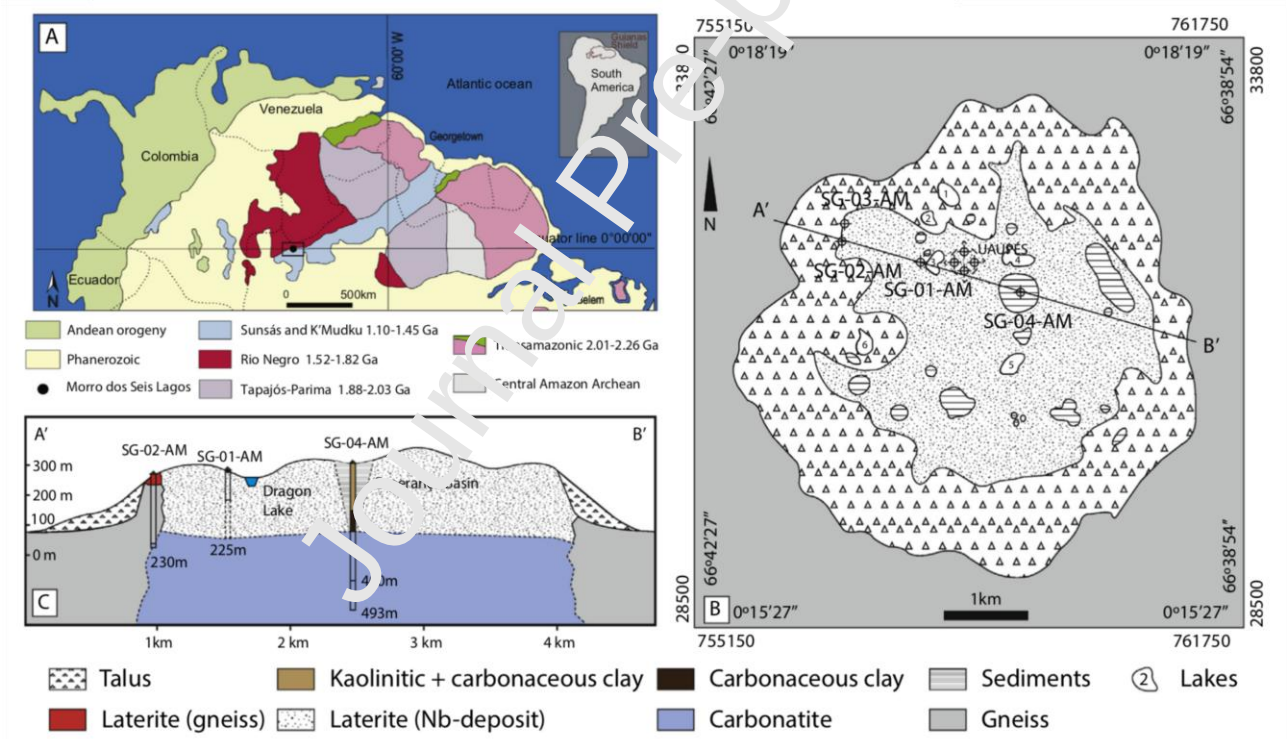

Figure 1. From Giovannini et al., 2020: (a) Geological provinces of the Guiana shield (b) geological map (c) cross-section of the Morro dos Seis Lagos carbonatite body (from Giovannini et al., 2021).

2.3 Micrometric-scale chemical and spectroscopic analyses

Polished sections of six samples (fragmented laterite, upper purple laterite, manganiferous laterite, lower purple laterite, brown laterite, carbonatite) were made by impregnating chips in epoxy resin and polishing on cloth with diamond pastes.

Scanning electron microscope (SEM) equipped with a field emission electron gun (FEG) (Zeiss Ultra55, Sorbonne Université) operating at 15 kV was used to characterize the mineralogical texture of the polished sections with an angular selective backscatter (AsB) detector collecting backscattered electrons. A Bruker Quantax energy dispersive X-ray spectroscopy (EDS) system using an Oxford 30 mm^2 silicon drift detector (SDD) was used to analyze and map the chemistry of the mineralogical phases.

Electron wavelength dispersive microanalyses were performed at SCMEM, GeoRessources laboratory (Nancy, France) with an electron probe microanalyzer (EPMA). Analysis of pyrochlore and Nb-bearing Ti and Fe oxides have been performed using a CAMECA SX5 Tactis (LaB_6 source) and a CAMECA SX100 (tungsten filament source), respectively. Two programs were elaborated. Pyrochlores were analyzed at 15 keV and 20 nA. The quantification of Nb-bearing Ti and Fe oxides was performed at 15 keV and 12 nA. The standards used are albite for Na and Al, orthoclase for Si and K, wollastonite for Ca, $MnTiO_3$ for Mn and Ti, hematite for Fe, $SrSO_4$ for Sr, YPO_4 for Y, $LiNbO_3$ for Nb, $BaSO_4$ for Ba, Ta metal for Ta, $PbCrO_4$ for Pb, ThO_2 for Th, uraninite for U, and REE-bearing monazite ($REEPO_4$) for La, Ce, Nd and Sm.

In order to determine the nature of the Ti oxide polymorphs found in the laterite, Raman spectra were collected on polished sections using a continuous-wave Renishaw InVia Reflex Raman microspectrometer using an Ar^+ laser. Measurements were performed using a 532 nm solid-state laser focused on the sample through a Leica DM2500 microscope with a 50 x objective providing a ca. 2–3 µm spot size. A maximal 5mW laser power was delivered at the sample surface.

2.4 X-ray absorption spectroscopy

2.4.1 Data acquisition

X-ray absorption spectroscopy data at Nb $L_{2,3}$-edges and K-edge were collected on the LUCIA beamline (Vantelon et al., 2016) at SOLEIL (Saint-Aubin, France) and on the BM23 beamline (Mathon et al., 2015) at ESRF (Grenoble, France) synchrotron facilities, respectively. Two types of experiments were conducted. The first one is XAS performed on bulk samples pressed into pellets with cellulose. The second one is micro-XAS analysis on polished sections of five lateritic horizons and the siderite carbonatite. Polished sections were first analyzed by synchrotron-based X-ray micro-fluorescence to locate the regions of interest identified by SEM–EDS.

The acquisition of the L_3-edge XANES spectra was obtained at room temperature and under vacuum in fluorescence-yield mode using a Si(111) double-crystal monochromator crystal calibrated at the energy of the Nb L_3-edge using Nb_2O_5 compound (Bollaert et al. 2023a). Energy steps were (2, 0.2, 1) eV for energy ranges of (2,300–2,350), (2,350–2,400) and (2,400–2,455) eV, respectively, with a 1 s integration time. Two measurements per sample were sufficient to get an adequate signal-to-noise ratio and check for the reproducibility of the edge features. Micro-XANES analyses were conducted by focusing the beam with 4 total reflection mirrors in Kirkpatrick-Baez geometry providing a spot size of ca. 2.8 x 3.8 µm.

Bulk Nb K-edge XANES and EXAFS scans were collected from 18,800 to 19,600 eV at room temperature in fluorescence-yield step-by-step mode using a silicon drift diode detector (SDD). The scans were stopped at 19,600 eV due to the high Th contents in the samples resulting in the Th L_3-edge at ca.19,700. The incident beam was focused to 2 x 1 mm^2 on crushed pellets. Using a high-resolution Si(111) monochromator and a set of Pt-coated Kirkpatrick-Baez mirrors, the incident beam was focused to 3 x 3 μm^2 FWHM for micro-XAS analyses. Two spectra per sample were collected.

2.4.2 Data processing

XANES scans were merged and normalized and background subtracted using the Larch package (Newville, 2013). For comparative purposes, the value of E_0 was fixed to 2372 eV at the L_3-edge and 18 993 eV at the K-edge, corresponding to the maximum derivative of the spectra. Niobium L_3- and K-edge spectra were analyzed with a least-squares linear combination fitting implemented on Larch (Newville, 2013). The spectra were fitted with reference compounds consistent with the description of the Nb carriers present in the corresponding horizons of the weathering profile (Giovannini et al. 2017). It includes pyrochlore reference samples provided by the mineral collection of Sorbonne Université (Bollaert et al., 2023). Niobium-bearing rutile (TiO_2), hematite (Fe_2O_3), goethite (FeOOH) and cerianite (CeO_2) have been synthesized due to their scarcity in mineralogical collections. Their syntheses have been described in Bollaert et al., (2023a).

EXAFS data were background subtracted using a cubic spline function with rbkg parameter set to the default value of 1. The normalized EXAFS oscillations were k^3-weighted and Fast Fourier-transformed (FFT) from k-space to R-space to obtain a radial distribution function (RDF) around central Nb atoms. Before FFT calculation, a Kaiser-Bessel window with a Bessel weight (dk) of 2 was applied over the 2.5−10 $Å^{-1}$ k-range for Nb-bearing rutile and brookite analyses and over the 2.5−8 $Å^{-1}$ k-range for Nb-bearing goethite. Shell-by-shell fitting of the Nb K-edge EXAFS data was performed in k-space using backscattering phase and amplitude functions generated by the FEFF 8 code. The limit of the number of free parameters in EXAFS fits can be calculated by the Nyquist formula is $N_{idp} = (2\Delta k \Delta R/\pi) + 2$ (Stern, 1993). Seven parameters were fitted for a maximum degree of freedom of N_{idp}= 12.98 for Nb-bearing Ti oxides and N_{idp}= 10.05 for Nb-bearing goethite. Fit quality was estimated by a reduced χ_R^2 of the following form: $\chi_R^2 = \frac{N_{idp}}{N_{points}(N_{idp}-N_p)} \frac{1}{\epsilon^2} \sum \left[k^3 \chi_{exp}(k) - k^3 \chi_{calc}(k)\right]^2$, where N_{idp} is the number of independent parameters that can be estimated, N_p is the number of parameters evaluated in the fit, N_{points} is the

number of data points to fit and ε is the estimated quadratic average of the data noise (Newville and Ravel, 2020). The phase shift and amplitude functions of the examined paths were obtained by substituting the central atoms (Fe, Ti) for Nb. The first three single-scattering paths were taken into account in the fitting procedure. Fit parameters include the interatomic distances (R, in Å); a Debye-Waller factor (σ^2, in $Å^2$) which is a measure of the effects of structural and vibrational disorder on the EXAFS signal; and the difference between the theoretical threshold energy and experimentally determined threshold energy (ΔE_0, in eV). The S_0^2 parameter was fixed to 1. Estimates of the uncertainties on the fitted parameters are made according to the standard statistical treatment of experimental data (Bevington and Robinson, 1993; Newville and Ravel, 2020). Such derived uncertainties reflect the uncertainties and correlations between variables.

3. RESULTS

3.1 Bulk mineralogical and geochemical evolution along the profile

In the core siderite carbonatite, Rietveld refinement of XRD patterns (Fig. 2b) indicates that siderite is the main mineral (64 wt %), followed by hematite (20 wt%), gibbsite (7 wt%), goethite (5 wt%) and rutile (3 wt%). The high signal-to-noise ratio provided by synchrotron-based HR-XRD allows the detection of albite, florencite ($CeAl_3[PO_4]_2(OH)_6$), and pyrochlore in low proportion (< 1 wt%). The weathering profile is dominated by Fe oxides all along the profile (50–90 wt%). Goethite is dominant in most samples (30–90 wt%). The proportion of hematite is significant in the manganiferous, upper purple, and fragmented horizons reaching (25 – 60 wt%) compared to the other horizons (< 10 wt%). Rutile and brookite are scarce in the lower purple horizon (< 1 wt%). They reach 5–10 wt % in the upper horizons (Fig. 2b). The manganiferous laterite is characterized by the presence of hollandite ($Ba[Mn^{4+}_6Mn^{3+}_2]O_{16}$) (16 wt%) and cerianite (3 wt%) together with Fe oxides. Diffraction peaks corresponding to florencite are found in all samples with a maximum proportion occurring in the mottled laterite (reaching 3 wt%). A second REE-rich mineral,

bastnaesite ([Ce, La]CO_3F), is identified in the brown laterite. The mineralogical evolution observed in the selected samples is consistent with the overall mineralogical description of the profile (Giovannini et al., 2017).

The concentration of the major elements (Fe, Mn, Ti) is consistent with the mineralogical evolution of their main host, namely, hematite/goethite, hollandite, and rutile/brookite (Fig. 2b,c).The maxima of MnO and Ce contents in the manganiferous horizon (Fig. 2c) are related to the presence of Mn- and Ce-oxide-enriched veins. The concentrations of Th and Zr, also considered as chemical invariants (Braun et al., 1993, Freyssinet, 1994) exhibit comparatively fewer chemical variations compared to Ce. Notably, there is an increase in the Zr concentration within the reworked laterite, with zircon being the only identified host for Zr (Fig. 2c). The Nb concentration varies from 800 ppm (manganiferous horizon) to a maximum content (1300 ppm) found in the lower purple horizon (Fig. 2c). The evolution of the Nb concentration is not linear from the siderite carbonatite to the top horizon (Fig. 2c). There is a joint evolution between Nb and Ti concentrations, in particular above the manganiferous horizon, from which rutile and brookite are abundant (Fig. 2c).

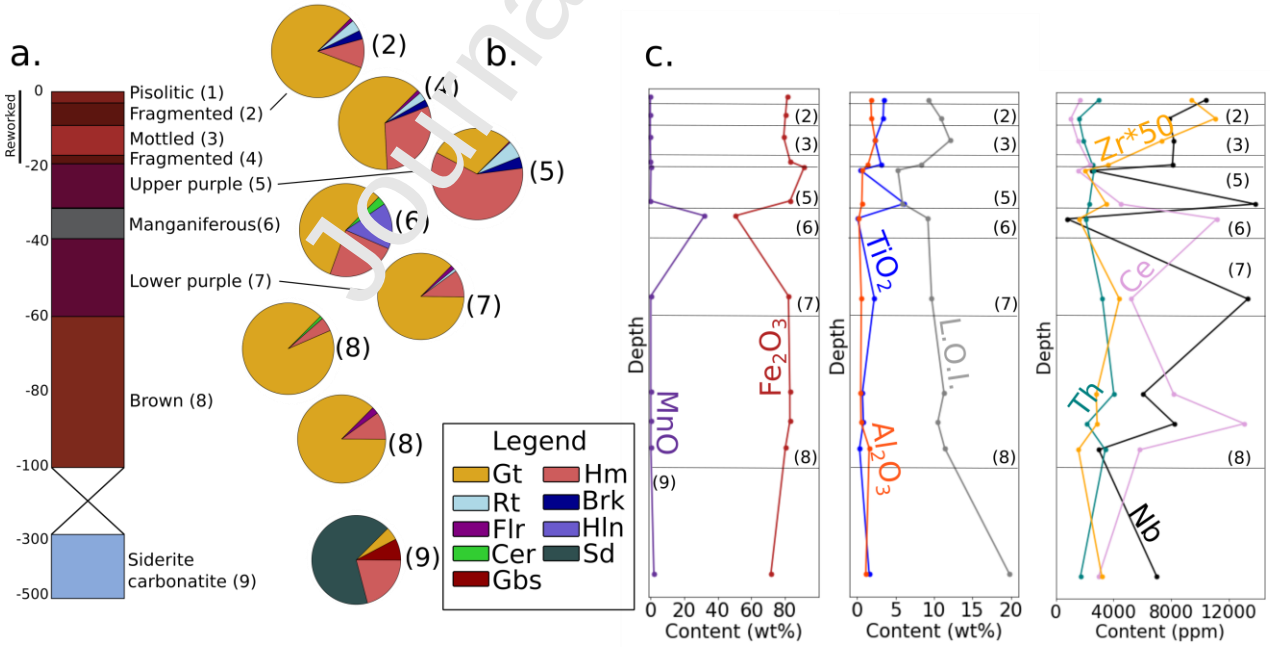

Figure 2. Mineralogical and geochemical evolution of the lateritic profile. (a) Schematic evolution

of the lateritic profile indicating the different horizons identified petrologically and their thickness. Horizons (1), (2), (3), (4) were subject to physical and chemical reworking. (b) Mineralogical proportions obtained by Rietveld refinement of HR-XRD patterns (Gt: goethite, Hm: hematite, Rt: rutile, Brk: brookite, Flr: florencite, Hln: hollandite, Cer: cerianite, Sd: siderite, Gbs: gibbsite). (c) Evolution of the concentrations of selected elements (MnO, Fe_2O_3, TiO_2, Al_2O_3, L.O.I in wt %, and Th, Ce, Nb, Zr in ppm) along the profile.

3.2 Characterization of the niobium carriers

3.2.1. Nature and distribution of the niobium carriers

The assessment of the relative abundance of the Nb hosts along the weathering profile was carried out using SEM and EPMA (Fig. 3). Their relative abundance varies depending on the horizons. Pyrochlore is dominant in the core carbonatite with rarer Nb-bearing Ti oxides. The presence of Nb-bearing goethite is inferred in the core carbonatite from EPMA analyses. Iron oxides are ubiquitous hosts for Nb in all the lateritic horizons. In the brown laterite, pyrochlore and Nb-bearing Ce oxides are readily detected whereas Nb-bearing Ti oxides are rarer. The lower purple horizon is characterized by the common occurrence of pyrochlore but the scarcity of Nb-bearing Ti and Ce oxides. In the manganiferous laterite, only hollandite and Ce oxides contain significant amounts of Nb. In the upper purple horizon, Nb-bearing phases are like that of the lower purple horizon, except for abundant Nb-bearing Ti oxides. In the fragmented horizon, pyrochlore and Ce oxides are rare while Nb-bearing Ti oxides are abundant.

Figure 3: qualitative relative abundance of Nb carriers as obtained by SEM and EPMA analyses. Relative abundances range from not observed to very abundant (+++) phases. The crystal-chemistry and the A-site occupancy of pyrochlore is mentionned in brackets.

3.2.2 Characterization of the Nb phases in the core siderite carbonatite

In the siderite carbonatite, Nb is hosted in a Ba-Ce-enriched pyrochlore which forms euhedral

(Fig. 4a) or partially broken crystals (Fig. 4b). In addition to high Ba and Ce concentrations (Fig. 5b), the crystal-chemical composition of pyrochlore (Table 1) is also characterized by minor amounts of Ti (3–5 wt% TiO_2), Fe (2–5 wt% Fe_2O_3), Si (2–6 wt% SiO_2), Pb (1–6 wt % PbO), La (1–2 wt% La_2O_3) and Nd (1–2 wt% Nd_2O_3). Their A-site occupancy is ranging between 0.6 and 0.8 apfu (Table 1).

Niobium-bearing Ti oxides form euhedral crystals of tens of microns (Fig. 4c) with oscillatory zoning (Fig. 4d). Rutile and brookite are both identifiable in the carbonatite using Raman spectroscopy (Fig. S3). Two varieties of Nb-bearing Ti oxides are distinguished based on their crystal-chemistry (Table 2). The first type is Nb-rich (12–21 wt% Nb_2O_5) and the second type is Nb-depleted (1–3 wt% Nb_2O_5) and K-rich (9–10 wt% K_2O). However, the variations of crystal-chemistry could not be associated with a specific spectroscopic signature related to rutile or brookite. Microprobe analyses also evidence the occurrence of Nb-bearing Fe oxide (Table 3) with significant Nb amounts (0.2–0.6 wt % Nb_2O_5) and low analytical totals (85–90 wt%).

Figure 4. Niobium carriers in the core siderite carbonatite. (a) Euhedral crystal of Ba-Ce pyrochlore

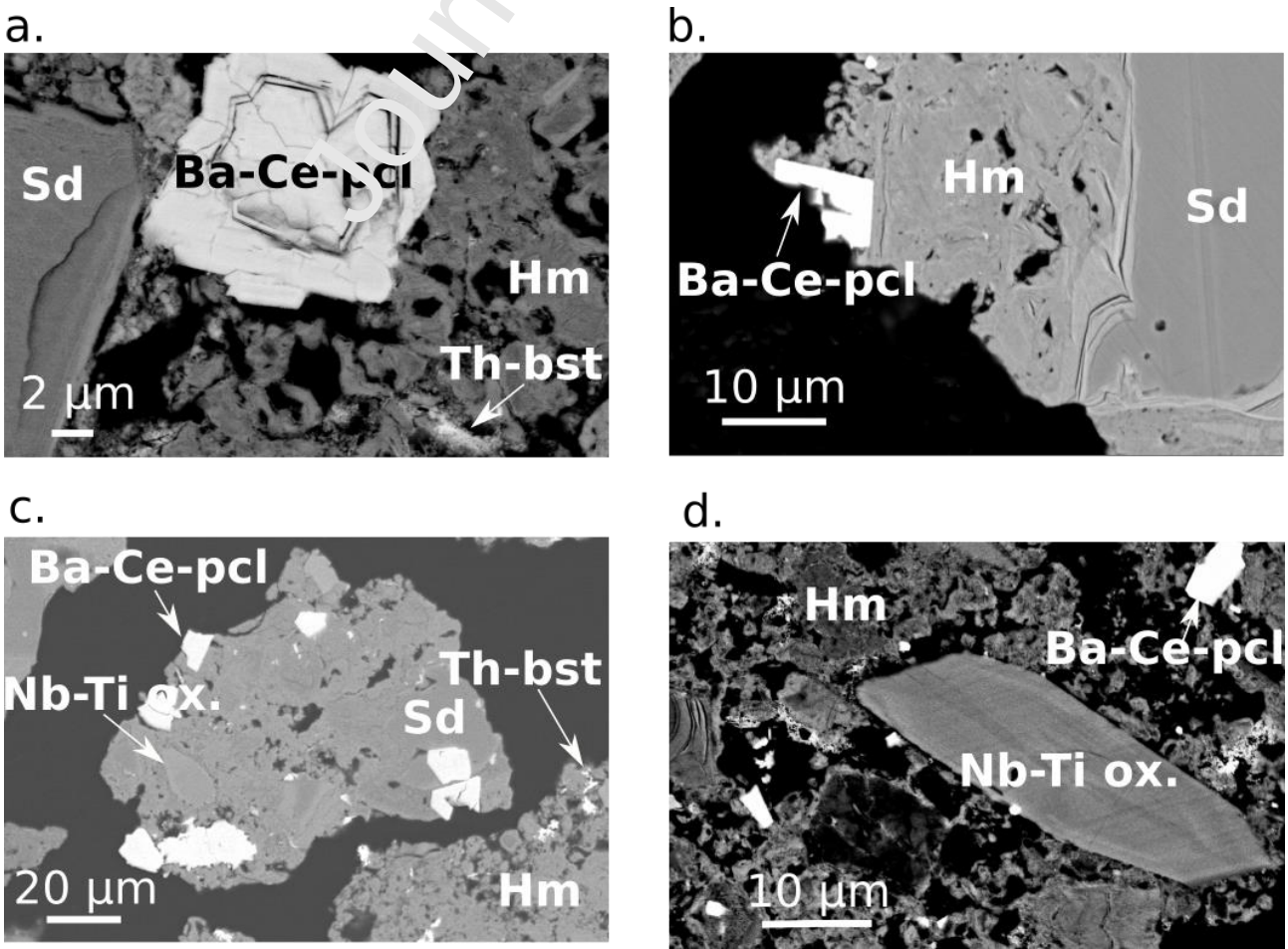

(Ba-Ce-pcl) in a siderite (Sd) and hematite (matrix) and aggregates of nanocrystals of Th-rich bastnaesite (Th-bst). (b) Broken Ba-Ce pyrochlore crystals in a hematite-rich matrix. (c) Niobium-bearing Ti oxide and Ba-Ce pyrochlore in a siderite grain. (d) Euhedral Nb-bearing Ti oxide crystal in a hematite-rich matrix.

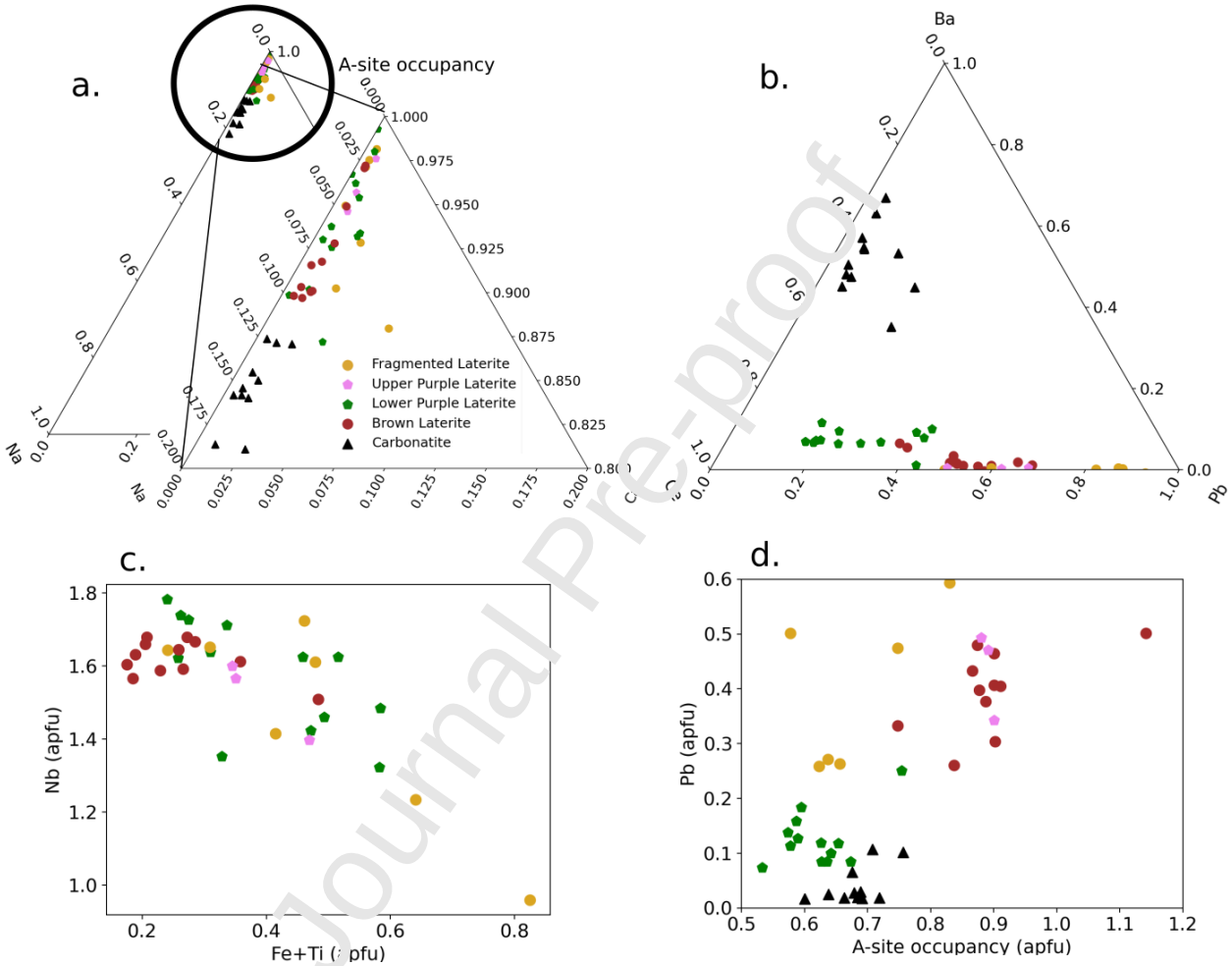

Figure 5. (a) Ternary plot of A-site occupancy, Na and Ca, and of (b) Ba, Ce, Pb in the studied pyrochlore. Binary diagrams of (c) Nb (apfu) vs Fe + Ti (apfu, (d) Pb vs A-site occupancy.

Table 1. Representative composition of pyrochlore from the core carbonatite and lateritic horizons using EPMA. The number after the name of the horizon of the sample corresponds to the number of the analysis.

wt%	Carb.8	Carb.12	Brown.2	Brown.10	Purple.2	Purple.11	Fragmented.9	Fragmented.5
A-site								
BaO	9.06	11.9	0.45	< d.l.	1.16	0.13	0.11	0.1
CaO	0.23	0.07	0.08	0.06	0	0.08	0.26	0.05
Ce_2O_3	9.9	9.79	14.82	14.17	11.46	12.59	8.7	3.45
K_2O	0.07	0.15	0.15	0.06	0.05	0.33	0.35	0.01
La_2O_3	1.86	1.8	0.38	0.56	2.92	1.86	1.95	1.98
Na_2O	1.63	0.85	0.56	0.16	0.03	0.1	0.29	0.12
Nd_2O_3	1.9	1.44	0.2	0.47	1.44	0.94	0.75	0.17
PbO	1.38	1.8	21.39	25.79	8.14	[illegible]	16.95	30.65
Sm_2O_3	0.36	0.16	< d.l.	< d.l.	0.08	< d.l.	0.13	< d.l.
SrO	0.33	0.19	0.05	< d.l.	< d.l.	< d.l.	< d.l.	0.03
ThO_2	0.33	0.19	0.05	< d.l.	< d.l.	[illegible]	4.23	4.19
Y_2O_3	0.16	0.17	0.13	0.03	1.4[illegible]	0.05	0.09	0.05
B-site								
Al_2O_3	0.17	0.19	< d.l.	< d.l.	[illegible]	0.11	0.14	< d.l.
Fe_2O_3	5.14	3.83	3.04	4.6	[illegible]	4.46	7.33	3.91
Nb_2O_5	54.53	59.61	55.66	54.48	52.91	42.16	48.62	49.52
TiO_2	4.59	3.09	0.75	0.48	[illegible]	3.55	7.02	0.01
SiO_2	4.0	2.19	0.02	[illegible]	0.17	0.6	1.65	2.18
Total	96.6	97.49	100.73	[illegible]	95.12	88.88	98.69	96.54
Normalization to 2 B-site cations								
A-site								
Ba	0.194	0.26[illegible]	0.012	0.000	0.029	0.004	0.002	0.003
Ca	0.013	0.004	[illegible]	0.004	0.000	0.007	0.016	0.004
Ce	0.189	0.1[illegible]	[illegible]	0.342	0.252	0.336	0.173	0.087
K	0.005	0.01[illegible]	0.014	0.005	0.004	0.032	0.025	0.001
La	0.037	0.03[illegible]	0.010	0.014	0.068	0.052	0.041	0.052
Na	0.17[illegible]	[illegible]	0.077	0.021	0.004	0.015	0.032	0.017
Nd	0.03[illegible]	0.029	0.005	0.012	0.032	0.026	0.015	0.004
Pb	0.02[illegible]	0.028	0.407	0.480	0.138	0.343	0.259	0.593
Sm	[illegible]	0.003	0.000	0.000	0.002	0.000	0.003	0.000
Sr	[illegible]	0.006	0.002	0.000	0.000	0.000	0.000	0.001
Th	[illegible]	0.002	0.001	0.000	0.000	0.090	0.055	0.068
Y	0.005	0.005	0.005	0.001	0.047	0.000	0.003	0.002
Total A-site	0.695	0.685	0.904	0.879	0.582	0.901	0.623	0.831
B-site								
Al	0.011	0.013	0.000	0.000	0.005	0.010	0.009	0.000
Fe	0.235	0.184	0.180	0.266	0.183	0.285	0.348	0.235
Nb	1.347	1.545	1.779	1.702	1.506	1.456	1.249	1.608
Ti	0.189	0.133	0.040	0.025	0.295	0.204	0.300	0.001
Si	0.219	0.126	0.001	0.008	0.011	0.046	0.094	0.157

3.2.3 Petrological and crystal-chemical evolution of pyrochlore along the profile

A diversity of pyrochlore morphologies and crystal-chemistry is evidenced using SEM and EPMA with variations between the horizons. In the brown laterite, micrometric-size agglomerates of pyrochlore are Pb-Ce-rich and partially hollowed by Nb-bearing Fe oxides (Fig. 6a,b). A mixed Nb-bearing Ce-Fe oxide pseudomorph is also found (Fig. 6). Pyrochlore A-site occupancy is higher than in the carbonatite (0.8–1.1 apfu). In the lower purple laterite, pyrochlore is Ce-Pb-rich (7–17 wt% CeO_2 and 5–11 wt% PbO). The composition of pyrochlore in the upper purple laterite is also enriched in Ce and Pb but it is characterized by the presence of Th (1–5 wt% ThO_2). Niobium-bearing Ti and Fe oxides pseudomorphs after pyrochlore are common in these horizons (Fig. 5d). The degree of alteration of pyrochlore in these horizons is variable ranging from slightly fractured to skeletal texture (Fig. 6e). In the fragmented laterite, pyrochlores are rare, display extensive alteration signs, and contain more Pb and less Ce than in the purple horizons. They exhibit concentric zones alternating with Nb-bearing Fe oxides (Fig. 6f). Pyrochlore is almost totally replaced by Nb-bearing Ti oxides pseudomorphs (Fig. 6f). In the fragmented laterite, pyrochlore displays the lowest A-site occupancy, comparable to the lower purple horizon (0.5–0.8 apfu).

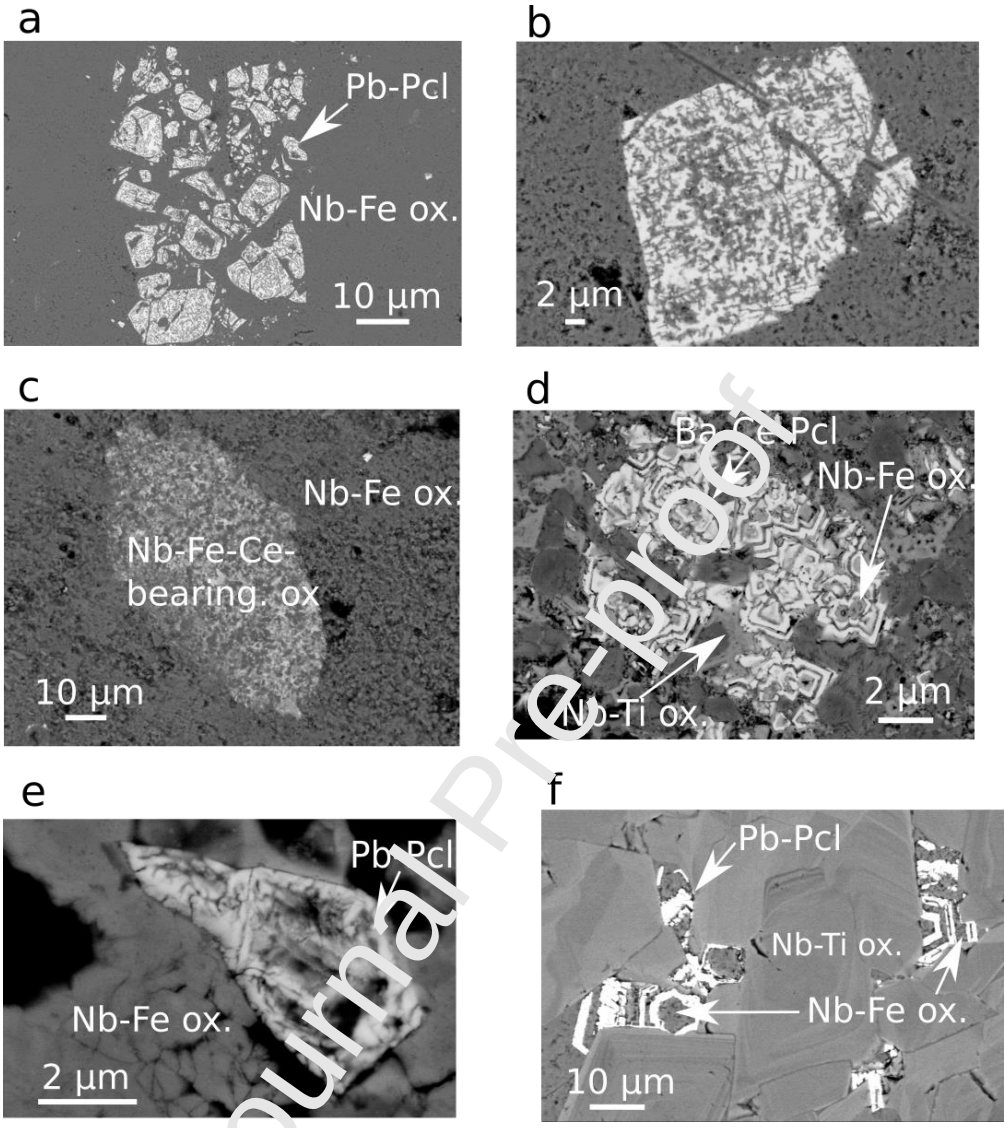

Figure 6. Illustration of the diversity of pyrochlore textures in the laterite. (a) Agglomerates of micrometric crystals of Pb-enriched pyrochlore (Pb-Pcl) hollowed by Nb-bearing Fe oxide (brown laterite). (b) Close-up on a weathered Pb-enriched pyrochlore crystal (brown laterite). (c) Pseudomorph of a mixed Nb-bearing Fe and Ce oxides after an unidentified mineral in an Nb-bearing Fe oxide-rich matrix (brown laterite). (d) Alteration of Ba-Ce-enriched pyrochlore (Ba-Ce-pcl) in concentric zones into Nb-bearing Ti and Fe oxides (purple laterite). (e) Skeletal crystal of

weathered Pb-enriched pyrochlore (fragmented laterite). (f) Replacement of Pb-enriched pyrochlore by zoned Nb-bearing Ti oxide (fragmented laterite).

The relative abundance of pyrochlore along the profile is monitored by the analysis of the HR-XRD patterns. The two main diffraction peaks of pyrochlore, corresponding to the [hkl] = [111] and [222] planes, are identified in the carbonatite, in the brown laterite and in the two purple horizons (Fig. 7). The position of these two diffraction peaks is shifted towards smaller inter-reticular distances with decreasing depth (Fig. 7). The difference in intensity between the two main peaks is greater in the brown laterite than in the other horizons.

Rietveld refinement was used to fit the position and relative intensities of the main diffraction peaks of pyrochlore. The crystallographic data were chosen according to their crystal-chemical composition (Table 1). Pyrochlore diffraction data from the core carbonatite is fitted using a Ba-bearing hydropyrochlore reference pattern (Miyawaki et al., 2021). The peaks corresponding to pyrochlore in the brown laterite are fitted with a hydroxyplumbopyrochlore reference pattern (Li et al., 2020). In the purple horizons, the relative intensities of the peaks can only be fitted with a mixture of two pyrochlores. In the lower purple horizon, Rietveld analysis indicates that Ce-bearing hydropyrochlore (Miyawaki et al., 2021) is more abundant than hydroxyplumbopyrochlore. Both pyrochlore species are found in equivalent proportions in the upper purple laterite.

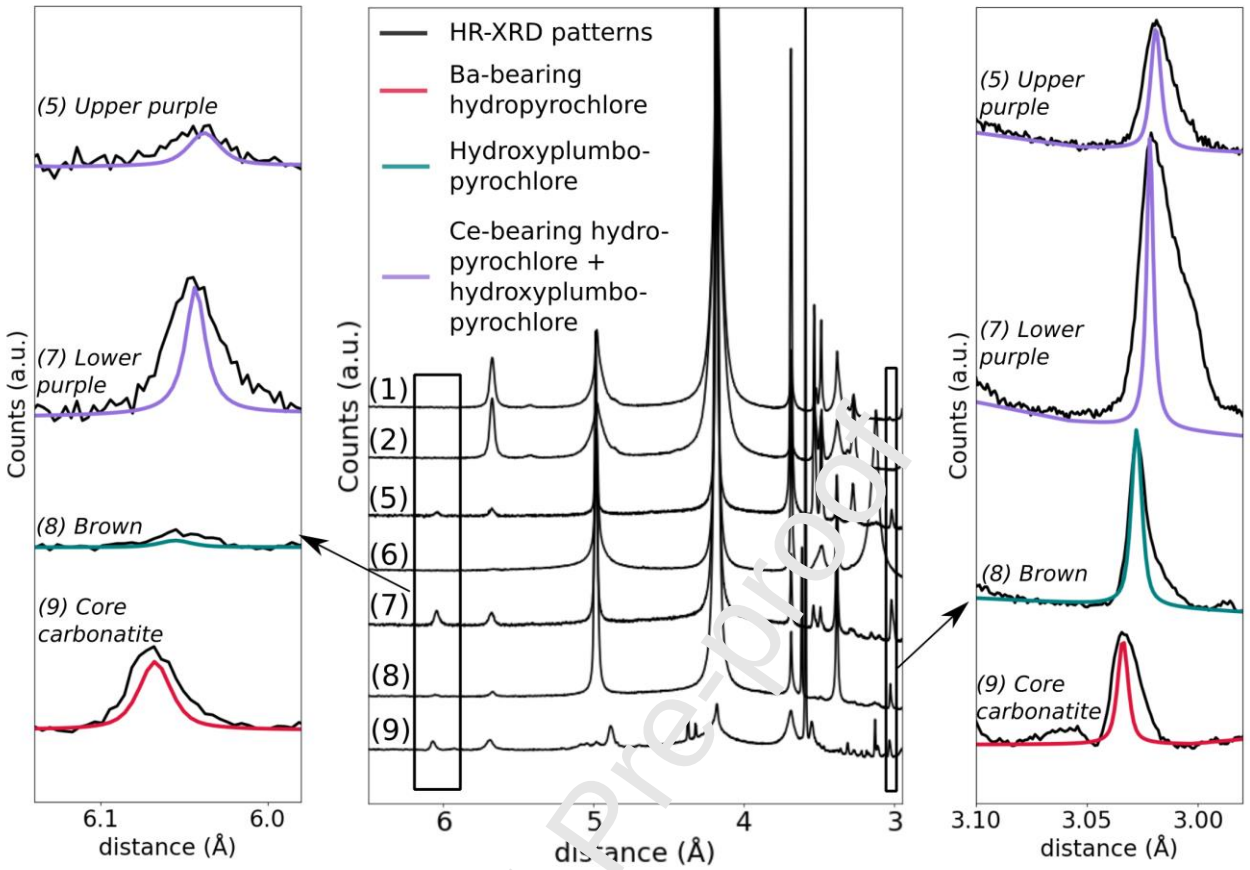

Figure 7. High-resolution XRD patterns obtained with synchrotron radiation of Morro dos Seis Lagos horizons (in black) compared with reference minerals (in color). The two main peaks corresponding to the [111] plane (6.0–6.1 Å) and [222] plane (3.0–3.05 Å) are fitted using references of pyrochlore with consistent composition with those from the Morro dos Seis Lagos profile. The larger width of the experimental peaks is ascribed to the crystal-chemical variability.

3.2.4 Petrological and crystal-chemical evolution of Nb-bearing oxides along the profile

In the brown laterite, Nb-bearing Ti oxide crystals exhibit a euhedral morphology and a size similar to primary Ti oxides found in the core siderite. They are partially replaced by Fe oxides in the laterite (Fig. 8a) or exhibit fractures (Fig. 8b). Porous square sections of Nb-bearing Ti oxides are also present, overgrown by successive rings of Nb-bearing Ti oxides (Fig. 8c). Micrometric-size

concentric zoning of Nb-bearing Ti oxides are very common in the laterite (Fig. 8d). The zoning, which also exhibits asymmetrical patterns (Fig. 8e), corresponds to variations in the Nb and Ti concentrations (Fig. 8f). The two types of zoning correspond to two distinct types of Ti oxides based on Raman analysis: the ones exhibiting concentric zoning are brookite, while the ones displaying asymmetric patterns are rutile (Fig. S4). The Nb contents in the rings (4 wt% Nb_2O_5), as obtained by SEM–EDS, are greater than in the center of this structure (1 wt% Nb_2O_5). Niobium-bearing Ti oxides pseudomorph at the expense of pyrochlore is a frequent feature of the fragmented horizon (Fig 8f).

The concentration of Nb in Ti oxides is between 12 and 27 wt% Nb_2O_5 in the laterite (Table 2). They also host Fe (7–15 wt% Fe_2O_3) and minor amounts of W and Al (< 1 wt% Al_2O_3 and WO_3). The concentration of Nb is moderately correlated with that of Fe ($r = 0.43$, $n = 49$) and the concentration of Nb+Fe is negatively correlated to that of Ti ($r = -0.89$, $n = 49$) (Fig. S5).

Diffraction peaks of Nb-bearing rutile and Nb-bearing brookite exhibit significant shifts compared to their pure counterparts (Fig. S6c,d). The (210) peak of brookite is shifted to + 0.2–0.3 Å depending on the horizons (Fig. S6c). Above the manganiferous horizon, the (110) peak of rutile is shifted to + 0.3–0.4 Å (Fig. S6d). Typical unit-cell parameters of Nb-bearing rutile ($a = b = 4.627$ Å, $c = 2.989$ Å) and Nb-bearing brookite ($a = 9.224$ Å, $b = 5.477$ Å, $c = 5.166$ Å) obtained through Rietveld refinement are larger than their pure counterparts ($a = b = 4.593$ Å, $c = 2.959$ Å for rutile and $a = 9.174$ Å, $b = 5.449$ Å, $c = 5.138$ Å for brookite) (Meagher and Lager, 1979).

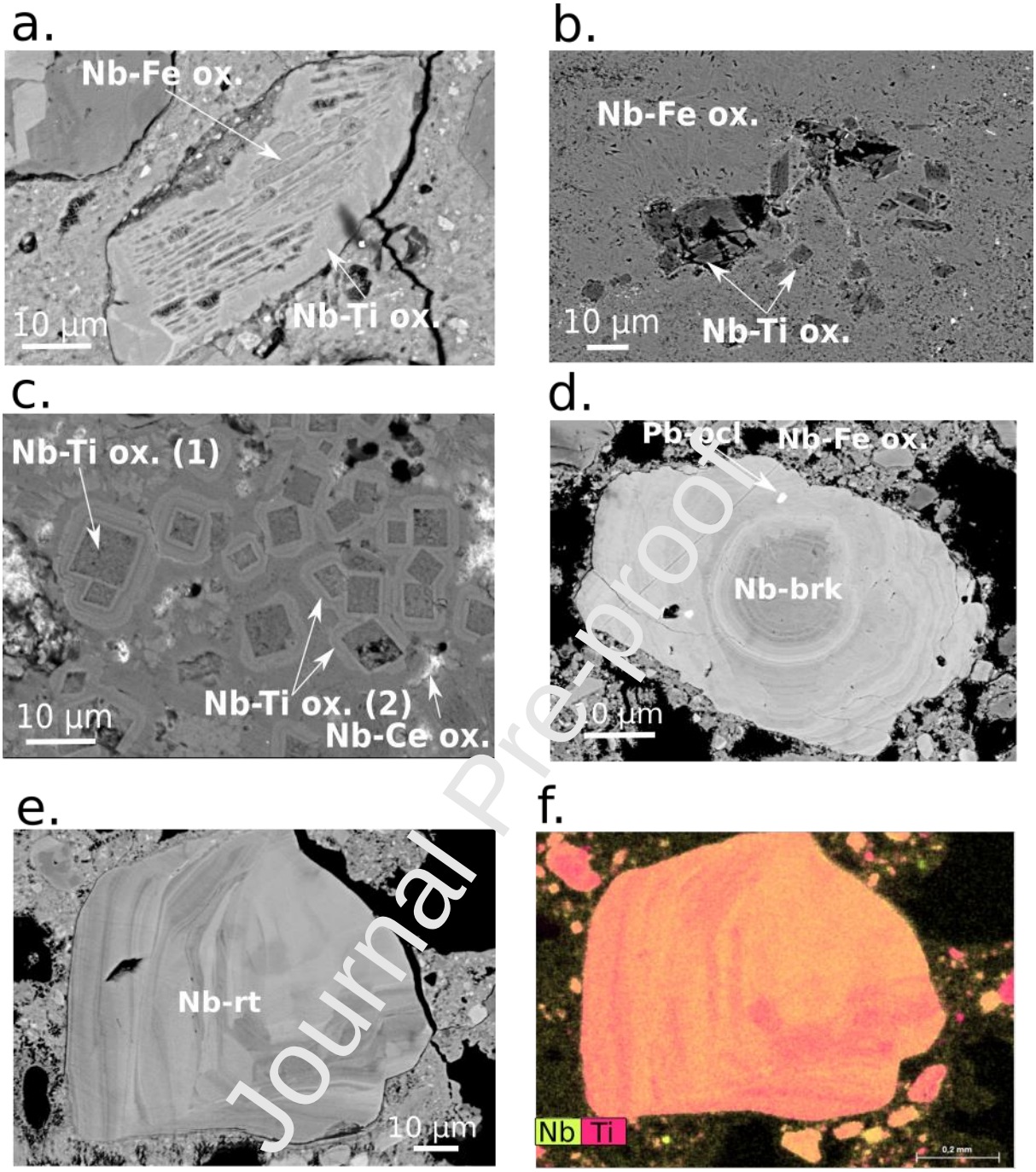

Figure 8. Illustration of the variety of Nb-bearing Ti oxides within the laterite. (a) Euhedral Nb-bearing Ti oxide partially altered into Nb-bearing Fe oxide. (b) Relics of primary Nb-bearing Ti oxides. (c) Porous square sections of Nb-bearing Ti oxide (Nb-Ti ox. 1) overgrown by successive generations of Nb-bearing Ti oxide (Nb-Ti ox. 2). (d) Zoned Nb-bearing brookite (Nb-brk) with inclusions of Pb-bearing pyrochlore (Pb-Pcl). (e) Neoformed Nb-bearing rutile (Nb-rt) displaying Nb and Ti zoning as evidenced by EDS chemical map (f).

Table 2. Representative compositions of Nb-bearing Ti oxides using EPMA. No Ti oxides have been analyzed in the brown laterite. The number after the name of the horizon of the sample corresponds to the number of the analysis.

wt%	Carb.1	Carb.13	Purple.27	Purple.25	Fragmented.24
Al_2O_3	< l.d.	0.10	0.02	0.06	0.59
Fe_2O_3	12.36	8.31	12.23	11.86	13.25
K_2O	9.21	0.49	0.34	0.49	0.38
MnO	0.10	0.06	< l.d.	< l.d.	< l.d.
Nb_2O_5	2.20	12.43	15.62	16.80	20.12
P_2O_5	0.09	0.43	0.21	0.25	0.41
SiO_2	0.17	0.04	0.66	0.82	0.64
TiO_2	77.65	77.62	70.59	68.97	65.38
WO_3	< l.d.	1.78	0.67	< l.d.	0.37
Total	101.6	101.26	100.93	98.62	101.13
Normalization to 2 oxygens					
Al	0.000	0.002	0.000	0.001	0.010
Fe	0.124	0.088	0.132	0.130	0.143
K	0.164	0.009	0.006	0.009	0.007
Mn	0.002	0.001	0.000	0.000	0.000
Nb	0.012	0.079	0.101	0.106	0.131
P	0.000	0.003	0.001	0.002	0.002
Si	0.002	0.001	0.009	0.013	0.009
Ti	0.838	0.821	0.760	0.753	0.706
W	0.003	0.007	0.003	0.000	0.001

Iron oxides form a ubiquitous fine-grained matrix in the weathered horizons (Fig. 9a,b). They host low but significant amounts of Nb (0.48 wt% Nb_2O_5 in average). The maximum concentration of Nb is 2.8 wt% Nb_2O_5 (Fig. 10a). There is a correlation between Nb and Ti in Fe oxides, although the slopes of these correlations vary between horizons. In the fragmented laterite, the Nb concentration in Fe oxides is positively correlated with Ti concentration (with a correlation

coefficient of r = 0.79, n = 140) (Fig. 10a). The coefficient of the linear regression is ca. 1. In the purple laterite, the coefficient of the linear regression is approximately 0.4 (with r = 0.56, n = 225). Niobium is also correlated with Si only in the Fe oxides analyzed in the purple horizon (Fig. 10b).Among Fe oxides, EPMA analyses reveal two clusters distinguished from their analytical totals (Table 3). A first cluster, representing 10 % of the analyses exhibits analytical totals above 95 wt% while Fe oxides from the second cluster have analytical totals between 80–95 wt% (Fig. 10c). The average Nb concentration in Fe oxides with high analytical totals is 0.33 wt % Nb_2O_5 while those with lower totals have an average of 0.67 wt % Nb_2O_5 (Fig. 10c). A third class of euhedral Fe oxides (Fig. 9a,b,c,d) with high analytical totals (97- 100 %) has Nb contents below the detection limit of EPMA. The concentration of Nb in Fe oxides is also variable along the profile with higher Nb content in the lowermost part of the profile (0.08 wt% Nb_2O_5) compared to the top profile (0.39 wt% Nb_2O_5) (Table 3). Iron oxides from the manganiferous horizon (Fig. 10) are distinguished by an average concentration of Nb close to the detection limit of EPMA (ca. 0.2 wt% Nb_2O_5).

The XRD peaks corresponding to goethite are shifted towards higher d-spacing in the 0.05–0.1 Å range in all horizons (Fig. S6a). The unit-cell parameters of Nb-bearing goethite as obtained by Rietveld refinement in the lower purple horizon are a = 4.607 Å, b = 9.960 Å and c = 3.023 Å while they are a = 4.598 Å, b = 9.951 Å and c = 3.018 Å in pure goethite (Yang et al., 2006). By contrast, the XRD peaks of hematite are not significantly shifted compared to their expected values in pure hematite (Fig. S6b).

Cerianite hosts low amounts of Nb (ca. 0.5–1.0 wt% Nb_2O_5), regardless of the horizon. Niobium-bearing cerianite forms intrusions and fills cavities of the Fe oxides matrix (Fig. 8a). Niobium-bearing cerianite is found in association with Fe oxides (Fig. 8e) or as dispersed micrometric crystals (Fig. 9f).

Niobium was detected in hollandite, abundant in the veins of the manganiferous horizon. The

Nb concentration, which varies from 0.2–0.4 wt% Nb_2O_5 is positively correlated with that of Fe_2O_3 (r = 0.75, n = 13) and negatively correlated with MnO (r = -0.76, n = 13).

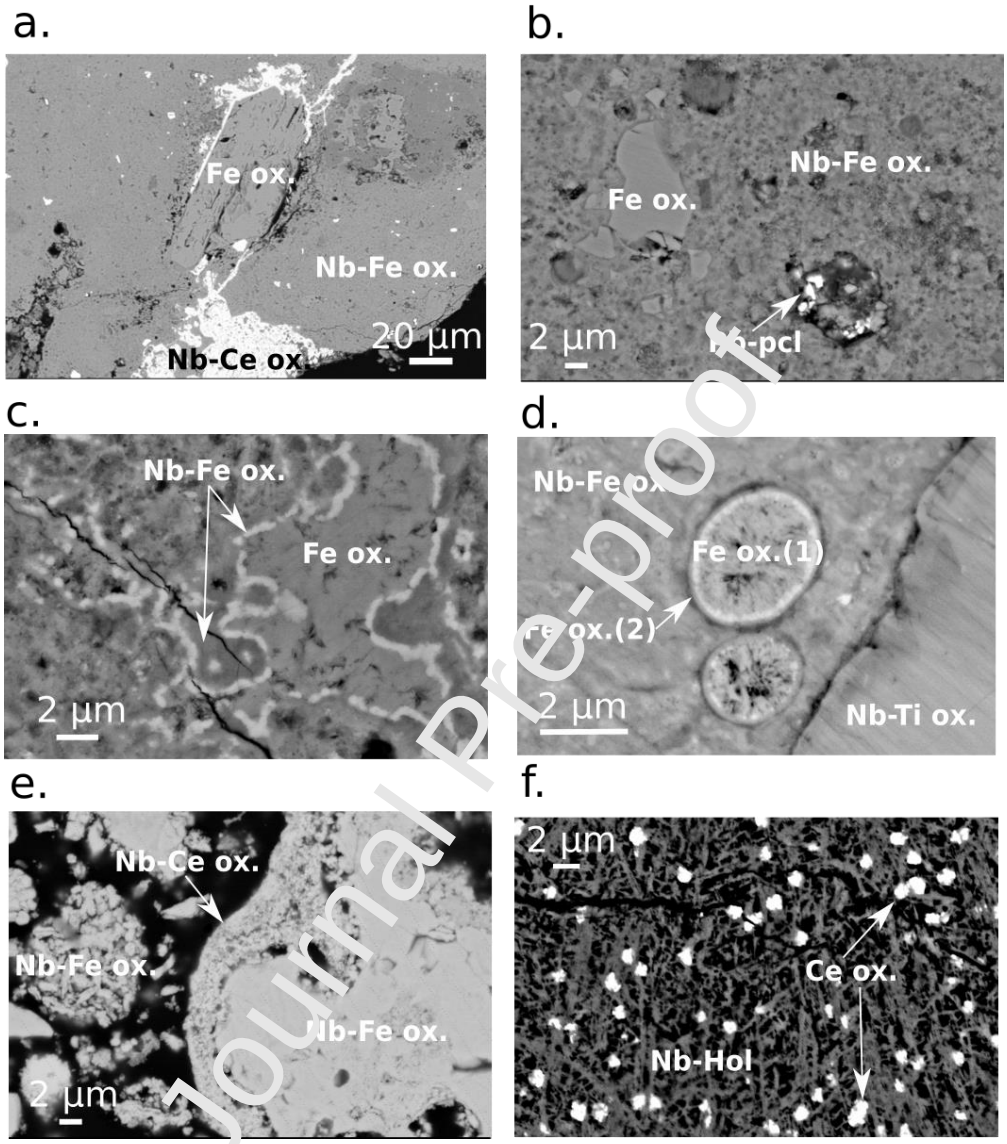

Figure 9. Typical features of the Nb-bearing Fe and Ce oxides in the laterite. (a) Euhedral Nb-free Fe oxide in an Nb-bearing Fe oxide matrix. Cavities are infilled by Nb-bearing cerianite (Nb-cer). (b) Fragmented Nb-free Fe oxide in a heterogeneous matrix of Nb-bearing Fe oxide. A residual Pb-enriched pyrochlore (Pb-pcl) is visible. (c) Banded Nb-bearing Fe oxide surrounding Nb-free Fe oxide. (d) Cross section through a Fe oxide nodule showing two generations of Fe oxides in a Nb-enriched Fe oxides matrix. (e) Niobium-bearing cerianite microcrystallites coating around Nb-bearing Fe oxides. (f) Dispersed micrometric-size cerianite within Nb-bearing hollandite (Nb-hol).

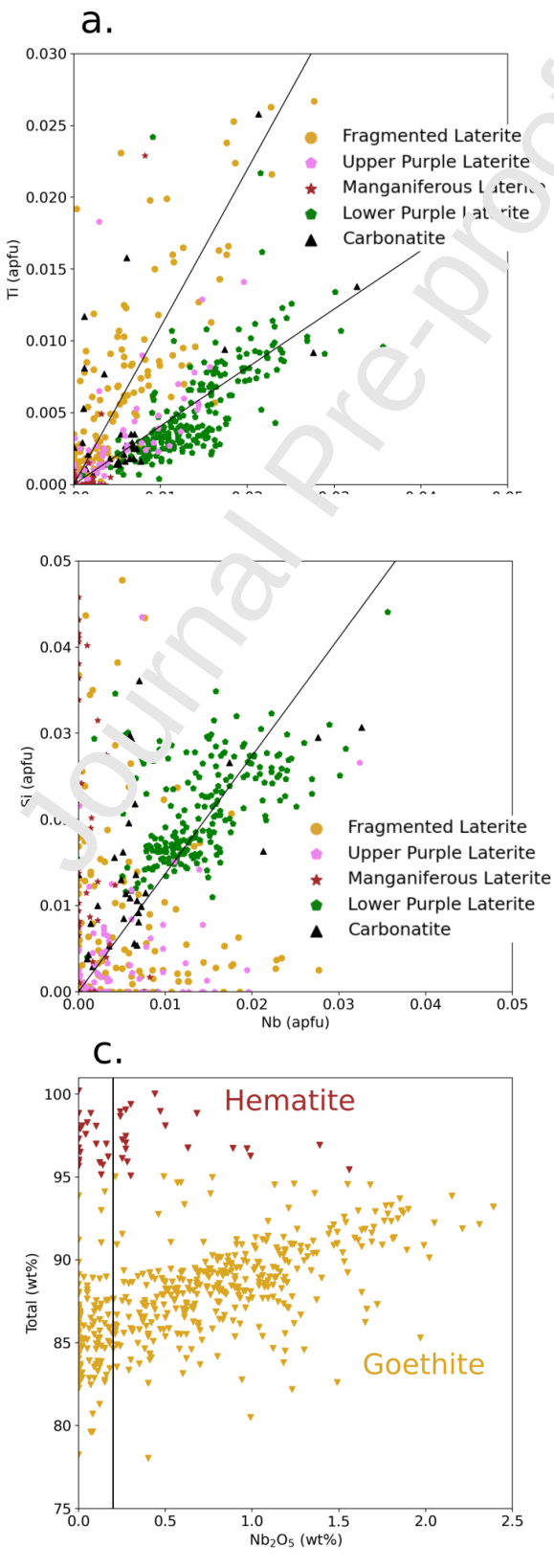

Figure 10. Bivariate plots of the concentrations of selected elements in the studied Fe oxides. (a) Ti (apfu) vs Nb (apfu), (b) Si (apfu) vs Nb (apfu), (c) analytical total vs Nb_2O_5,The vertical black line indicates the limit of detection of Nb. The standard deviation on the Nb concentration is ca. 0.2 wt % Nb for Fig. 10c.

Table 3. Representative compositions of Nb-bearing Fe oxides using EPMA. The number after the name of the horizon of the sample corresponds to the number of the analysis.

wt%	Carb.16	Lower Purple.157	Mangan.15	Mangan.44	Upper Purple.11	Upper Purple.65	Fragmented.95
Al_2O_3	1.44	0.35	1.39	0.53	0.20	1.32	1.59
Fe_2O_3	85.85	84.57	83.53	83.17	88.20	97.09	84.5
K_2O	<l.d.	<l.d.	0.01	<l.d.	<l.d.	0.02	<l.d.
MnO	0.03	0.47	0.22	0.53	0.37	<l.d.	<l.d.
Nb_2O_5	0.50	0.99	<l.d.	0.17	0.16	0.27	0.57
P_2O_5	0.15	<l.d.	<l.d.	0.00	< l.d.	0.24	1.25
SiO_2	0.18	0.61	1.53	0.68	0.07	0.15	<l.d.
TiO_2	0.13	0.25	0.02	< l.d.	< l.d.	< l.d.	0.33
WO_3	< l.d.	< l.d.	0.21	< l.d.	< l.d.	< l.d.	0.05
Total	88.27	88.11	86.92	85.10	89.00	99.08	88.31
Normalization to 3 oxygens							
Al	0.051	0.012	0.049	0.019	0.007	0.041	0.056
Fe	1.924	1.925	1.883	1.939	1.980	1.943	1.895
K	0.000	0.000	0.000	0.000	0.000	0.001	0.000
Mn	0.001	0.012	0.006	0.014	0.009	0.000	0.000
Nb	0.007	0.014	0.000	0.002	0.002	0.003	0.008
P	0.002	0.000	0.000	0.000	0.000	0.003	0.016
Si	0.005	0.018	0.046	0.021	0.002	0.004	0.000
Ti	0.003	0.006	0.000	0.000	0.000	0.000	0.007
W	0.000	0.000	0.002	0.000	0.000	0.000	0.000

3.3 Spectral properties of Nb carriers

The atomic environment of Nb in the phases of the Morro dos Seis Lagos laterite has been characterized using micro-focused Nb L_3- and K-edges XANES and EXAFS spectroscopies on the variety of grains identified through SEM and compared with spectra of mineral references. Niobium XANES spectra of Morro dos Seis Lagos pyrochlore match the spectra of hydropyrochore and Ba-bearing kenopyrochlore of reference at both edges. The Morro dos Seis Lagos Nb-bearing goethite spectra match the spectral features of Nb-bearing goethite reference, although the pre-edge of the reference at the K-edge is of lower intensity (Fig. 11). We collected two distinct spectra corresponding to Morro dos Seis Lagos Nb-bearing Ti oxides at the Nb L_3-edge. Their spectral features are distinct from those of Nb-bearing rutile reference (Fig. 11). At the K-edge, the spectrum of several Ti oxide grains matches that of Nb-bearing rutile reference. Spectra acquired on Nb-bearing Ti oxide with concentric zoning are distinct (Fig. 11). They correspond to Nb-bearing brookite as indicated by Raman spectroscopy (Fig S4). Niobium-bearing cerianite has only been characterized at the L_3-edge (Fig. 11). The spectra of Morro dos Seis Lagos and reference cerianite display significant differences regarding their energy position and relative intensities. This discrepancy can be explained by a mixing of the spectroscopic signal with the one of neighbor Fe-

oxides (Fig. S7).

We performed a shell-by-shell fit analysis of the micro-EXAFS data at the Nb K-edge of rutile, brookite and goethite to investigate the local structural environment of Nb (Fig. 12). The EXAFS data of Nb-bearing rutile are fitted with octahedrally-coordinated Nb with an average Nb–O distance of 1.95 Å (Table 4). The second and third contributions visible in the FFT spectrum (Fig. 12b) are fitted with 2 Nb–Ti (3.02 Å) and 8 Nb–Nb (3.39 Å) paths. The first two distances are consistent with those obtained from previous EXAFS analysis of Nb-substituted rutile but the third distance is shortened by ca. 0.2 Å (Table 4). This discrepancy with the reference spectrum is marked in the k^3-weighted EXAFS spectrum in the 5–10 $Å^{-1}$ k-range (Fig. 12a). At this k-range, the spectrum of micro-focused rutile is closer to that of micro-focused brookite. The first contribution in the FFT spectrum of Morro dos Seis Lagos brookite is fitted with 6 oxygen atoms at 1.97 Å. The second contribution is fitted with 4 Nb–Ti/Nb distinct paths ranging from 2.75–3.43 Å, mirroring the complex medium-range structure of brookite. The EXAFS data of goethite from the studied profile are fitted with one Nb–O path at 1.95 Å and two Nb–Fe paths at 3.09 and 3.61 Å. The local atomic environment of Nb in goethite from Morro dos Seis Lagos is consistent with the Nb site geometry found in synthetic Nb-substituted goethite (Bollaert et al. 2023b).

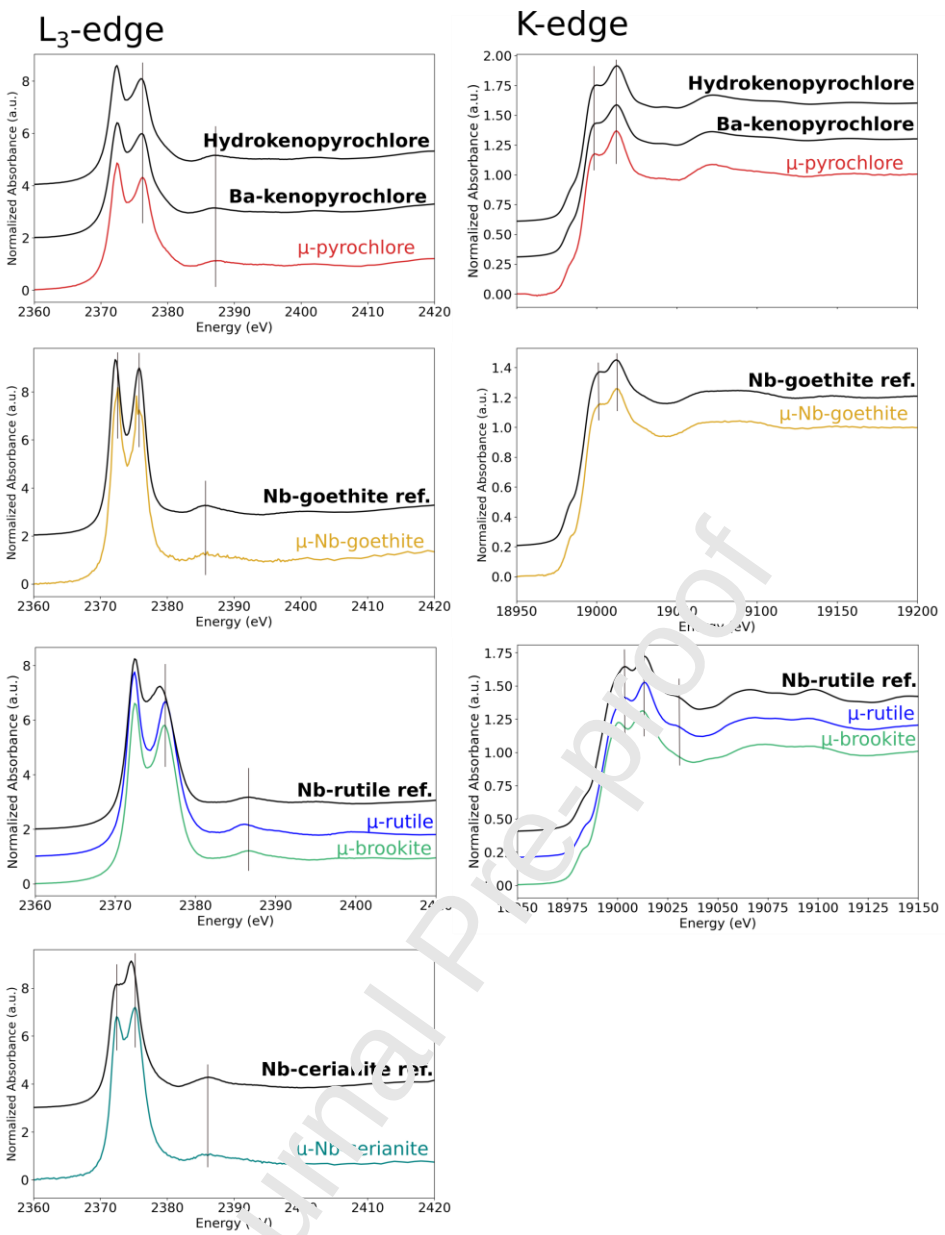

Figure 11. Comparison of the Nb L_3- and K-edge XANES spectra of the Nb-bearing minerals identified at Morro dos Seis Lagos with their associated reference materials The spectrum of Nb-bearing cerianite has not been collected at the K-edge.

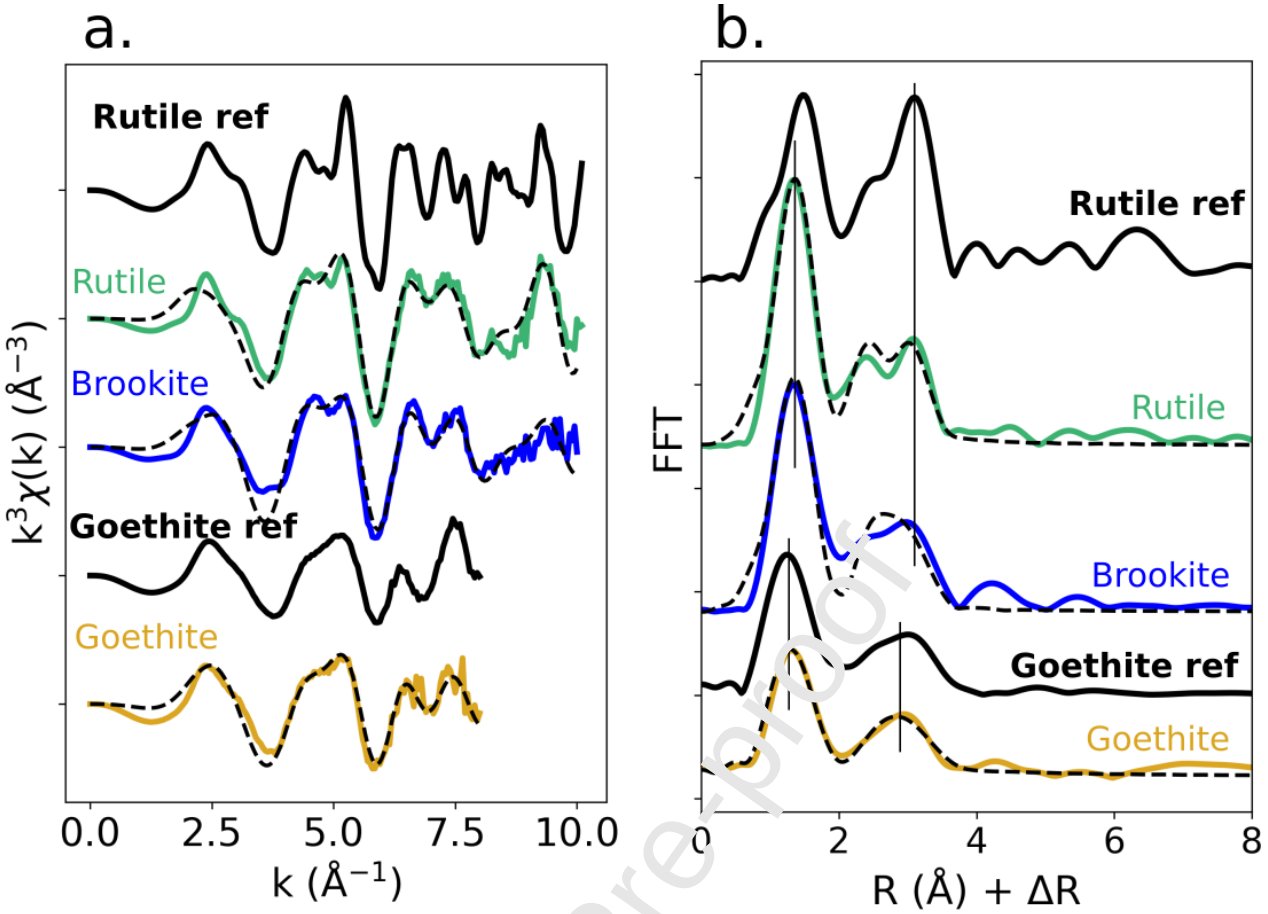

Figure 12. (a) Background-subtracted, normalized, and k^3-weighted Nb K-edge EXAFS spectra and (b) fast Fourier transforms of micro-focused rutile, brookite and goethite collected in the weathering profile. Fits of these spectra are shown as black dashed lines. Structural details resulting from the fit are reported in Table 4. The EXAFS data of reference Nb-substituted rutile and goethite are shown as solid black lines (Bollaert et al., 2023b).

Table 4. Results of the shell-by-shell fits of Nb K-edge EXAFS data for micro-focused rutile, brookite and goethite from the weathering profile. R_{calc}(Å): calculated interatomic distance, R_{ref} (Å): expected Ti–O and Fe–O interatomic distances in pure oxides; N: number of neighbors; ΔE_0 (eV): difference between the user-defined threshold energy and the experimentally determined threshold energy; σ^2 : Debye–Waller factor, ΔE the experimentally determined threshold energy, in electronvolts; χ^2 : goodness of fit. Fit quality is estimated by a χ^2 value and uncertainties on reported parameters are given under bracket. The S_0^2 parameter was fixed to 1.

Sample	R_{calc} (Å)	R_{ref} (Å) pure	N	σ (Å²)	ΔE_0 (eV)	χ^2_R
Nb rutile	1.95 (± 0.009)	1.947–1.982	6.0 Nb–O	0.008 (± 0.0006)	-5.70 (± 0.7)	1.59
	3.02 (± 0.015)	2.96	2.0 Nb–Ti	0.003 (± 0.001)	–	
	3.39 (± 0.015)	3.57	8.0 Nb–Nb	0.012(± 0.001)	–	
Nb brookite	1.95 (± 0.02)	1.86–2.05	6.0 Nb–O	0.012 (± 0.001)	-8.95 (± 1.7)	2.74
	2.82 (± 0.10)	2.95	3.0 Nb–Nb	0.014 (± 0.002)	–	
	3.57 (± 0.05)	3.52	4.0 Nb–Ti	0.009 (± 0.002)	–	
Nb goethite	1.95 (± 0.05)	1.93–2.11	6.0 Nb–O	0.017 (± 0.0009)	-7.27 (± 0.7)	1.52
	3.09 (± 0.07)	3.02	3.0 Nb–Fe	0.011 (± 0.0004)	–	
	3.61 (± 0.16)	3.45	3.0 Nb–Fe	0.016 (± 0.0012)	–	

3.4. Evolution of the average niobium speciation

The average Nb speciation was studied along the weathering profile using XANES spectroscopy at the Nb L_3- and K-edges on Morro dos Seis Lagos powdered bulk samples (Fig. 13). The powdered bulk spectra have been fitted using spectra of mineral references representative of the identified Nb-bearing phases: Ba-bearing kenopyrochlore (Pcl), goethite (Gt), hematite (Hm) and cerianite (Cer). Since the spectrum of Nb-bearing rutile reference was not representative of Nb-bearing rutile in the Morro dos Seis Lagos profile, we use instead the micro-focused spectrum of Nb-bearing rutile (Rt) as a fitting component (Fig. 11). Given the absence of a reference for Nb-bearing brookite, the micro-focused L_3-and K-edge spectra identified as brookite (Brk) were used as a fitting component.

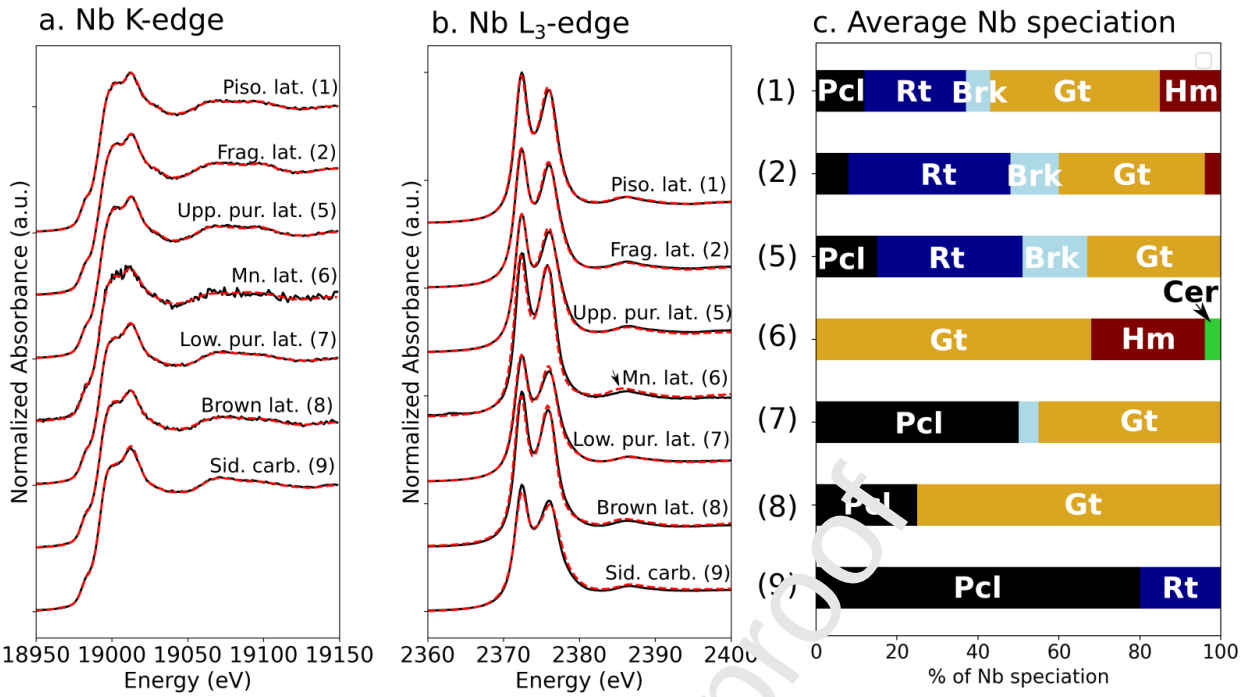

Figure 13. Evolution of the average Nb speciation along the weathering profile. Least-squares linear combination fitting results at the (a) Nb K-edge and (b) L_3-edge. Experimental spectra and fits are displayed as solid black and dashed red lines, respectively. (c) Proportions of the fitting components corresponding to the average Nb speciation. Uncertainties on the fitting components as given by the Larch package are ± 2–3 %.

The Nb K-edge XANES spectra were fitted in the first place (Fig. 13a) given the clear differences occurring between Nb-bearing goethite and hematite spectra (Bollaert et al., 2023b) and between Nb-bearing brookite and rutile (Fig. 11). Globally, the contribution of pyrochlore to the average Nb speciation progressively decreases (Fig. 13c) from the carbonatite (80 %) to the fragmented laterite (8 %). The lower purple horizon is an exception to this trend with a greater proportion of pyrochlore (45%) than in the brown laterite (25 %) underneath (Fig. 13c). In the lowermost profile, the contribution of Nb-bearing Ti oxides is weak while it is significant in the parent carbonatite (20 %). By contrast, rutile and brookite together contribute to about half of the Nb speciation in the uppermost laterite (30–50 %). The contribution of Nb-bearing Fe oxides is

significant in all the horizons of the profile (33–95 %) (Fig. 13c). Among Fe oxides, goethite is the predominant Nb host relative to hematite. The best fit of the manganiferous horizon is obtained with Nb-bearing Fe oxides components and minor cerianite (4 %). The discrepancy pointed out at 2,385 eV may arise from the absence of a Nb-bearing hollandite spectrum of reference while this phase has been identified as a Nb host in this horizon.

The L_3-edge XANES spectra of the studied horizons are reproduced by using the proportions of the fitting components obtained at the K-edge (Fig. 13b), indicating the robustness of the average Nb speciation obtained (Fig. 13c).

4. DISCUSSION

4.1 Influence of the parent rock on the average Nb speciation in the lateritic profile

With increasing alteration, no consistent evolution in the A-site occupancy of pyrochlore is observed (Fig. 3, Table 1), in contrast with the expected increase in A-site vacancies. Beyond physico-chemical conditions of weathering, Nb speciation along the lateritic profile will depend on the nature of the parent rock (Braun et al., 1990; Estrade et al., 2019; Wu et al., 2023). The vertical progression of a weathering front within a homogeneous parent lithology is unlikely in the case of a hundred-meter-thick lateritic profile. The size of the carbonatite body and the position of the drilling relative to this intrusion imply that the parent rock is a carbonatite. Nonetheless, the carbonatite intrusion is at least composed of three facies with distinct mineralogy and chemistry: the border, core and REE-rich core siderite carbonatite (Giovannini et al., 2020). The border siderite carbonatite is composed of siderite, barite, gorceixite and rhabdophane-(Ce) whereas the core carbonatite is mainly composed of siderite and hematite. The REE-rich core carbonatite is similar to the core facies with monazite and bastnaesite. Due to the absence of a relevant geochemical proxy which could relate a given lateritic horizon to one of the facies (Fig. S1), we have chosen the composition of pyrochlore in the laterite to assess the parent rock heterogeneities of the weathering

profile.

The high A-site occupancy in pyrochlores observed in the brown laterite compared to the core carbonatite (Fig. 5d, Fig. 3) may indicate that the border siderite carbonatite, exhibiting pyrochlore with a high A-site occupancy is thus the potential facies of the brown horizon. The composition of pyrochlore in the lower purple laterite indicates its genetic link with the core siderite carbonatite (Fig. 3). The higher A-site occupancy of pyrochlore from the upper purple horizon (Fig. 3) suggests that it formed from facies similar to the one forming the brown horizon. The low average A-site occupancy of pyrochlore from the fragmented horizon (Fig. 3) is consistent with the advanced stage of weathering in this horizon resulting from the reworking of an earlier laterite. The veins from the manganiferous horizon with distinct chemical and mineralogical features (Fig. 2), do not result from the weathering of a specific parent lithology but stem from the migration and concentration of Mn^{2+}, Ce^{3+}, and Ba^{2+} into fractures.

As the profile is likely formed from various facies exhibiting chemical disparities, mass-balance calculations could not be conducted to estimate Nb mass loss or gains along the profile (Fig. S2). However, as the different facies have a similar Nb mineralogy dominated by pyrochlore with minor Ti oxides (Giovannini et al., 2020), the evolution of the average Nb speciation will primarily mirror the weathering processes at stake rather than reflecting heterogeneities within the parent carbonatite.

4.2 Evidence of niobium leaching and trapping during weathering

Although Ti oxides such as rutile and pyrochlore group-minerals are considered weathering-resistant in lateritic profiles (Milnes and Fitzpatrick, 1989; Nasraoui and Bilal, 2000), alteration features are evident from SEM imaging (Fig. 6). While primary Nb-bearing Ti oxides (brookite and rutile) are pristine in the parent rock (Fig. 4c,d), they are porous and fragmented in the lateritic horizons (Fig. 8a,b). Spectroscopic data even demonstrate the significant alteration of primary Nb-bearing Ti oxide in the least weathered horizon, the brown laterite (Fig. 13).

Pyrochlore grains from the laterite exhibit volume loss of about 30–50 % relative to the hollowed shape of the crystal (Fig. 6a,b). Some horizons even show volume loss higher than 90 % (Fig. 6f). These alteration features indicate the destabilization of the pyrochlore structure despite its expected resistance to alteration processes (Lumpkin et al., 2000). One of the hypotheses explaining the alteration of pyrochlore is the continuous leaching of A-site cations stabilized by the incorporation of H_2O and OH^- leaving behind an unstable Nb_2O_5 skeleton (Lumpkin and Ewing, 1995; Williams-Jones and Vasyukova, 2022). Nonetheless, the structure of pyrochlore can be preserved with 98 % vacancies in the A-site (Wall et al., 1996). Here, strong A-site depletion is not observed in the top laterite (Table 1, Fig. 3) although pyrochlore remainss as scarce fragments (Figs. 6, 13). A decrease in Nb is accompanied by an increase of the Fe+Ti content in the altered pyrochlores (r = -0.66, Fig. 5c) evidencing the replacement of Nb^{5+} by Ti^{4+} and Fe^{3+} in the B-site by supergene fluids. The Fe+Ti amounts can reach 0.3 to 0.7 apfu in the fragmented horizon showing that up to 25 % of the B-site can be affected. Although the B-site is considered to remain unchanged during weathering (Lumpkin and Ewing, 1995), unusual Fe and Ti concentrations have been identified in altered pyrochlores from laterites (Lottermoser and England, 1988; Nasraoui et al., 1999; Khan et al., 2021; Ribeiro da Costa et al., 2021). The substitution of *3d* elements like Fe and Ti for *4d* elements like Nb may weaken the structure due to the lower covalency of *3d* ions–O bonds compared to those formed with *4d* elements (de Groot et al., 1994). Such substitutions induced by intense weathering may have triggered the destabilization of the B_2O_6 octahedral framework and eventually, the collapse of the pyrochlore structure.

After the alteration of the primary Nb phases and the release of Nb into the fluids, the fate of Nb depends on the mineralogy of the horizon. In the brown and lower purple horizons, Nb is mostly hosted in goethite (Fig. 13), while Ti oxides (rutile and brookite) are the main hosts for Nb in the pisolitic, fragmented and upper purple horizons. In the brown horizon, the contribution of Ti oxides to the average Nb speciation is low due to the alteration of primary Ti oxides and limited

precipitation of secondary Ti oxides (Fig. 2c). In the absence of Ti oxides as is the case in the brown laterite, the Nb released from primary pyrochlore and Nb-bearing Ti oxides is scavenged by Fe oxides, especially goethite. In the upper purple laterite horizon and above, the formation of Ti oxides is coupled with an increase in the contribution of Ti oxides to Nb speciation (Fig. 13). In these horizons where both Ti and Fe oxides coexist, the Nb concentration in Fe oxides decreases (Table 3). This, along with the observed correlation between Nb and Ti bulk concentrations, highlights the preferential scavenging of Nb with Ti oxides.

In the manganiferous veins, the Nb content in Fe oxides remains below the detection limit of EPMA (0.15 wt% Nb). However, the resemblance between the spectra of the powdered bulk spectrum of the vein and Nb-bearing Fe oxide (Fig. 13) suggests the possibility of Nb being present in the latter, albeit in very low concentrations. Significant Nb contents are measured in hollandite (ca. 0.3 wt%) and cerianite (ca. 1 wt%), indicating that Mn and Ce oxides are efficient scavengers of Nb.

Overall, the alteration of Nb minerals from the parent rock combined to the variations in the average Nb speciation along the weathering profile demonstrates a mobilization of Nb from primary phases and further incorporation into secondary Fe and Ti oxides, and in specific conditions, in Ce and Mn oxides formed during weathering processes. Niobium mobilization occurs at the scale of the mineralogical assemblage in most of the weathering profile except in the Mn veins where the presence of Nb proves that its mobility extends to the profile scale.

4.3 Physico-chemical conditions favoring niobium mobilization

The mineralogy and crystal-chemistry of secondary oxides can be used to provide information on the geochemical conditions leading to Nb mobilization. The predominance of goethite along the entire profile, related to high water activity during laterite formation (Tardy and Nahon, 1985), reflects weathering under a seasonally wet tropical climate (Schwertmann, 1971). Electron

microscopy shows zoned Nb-bearing Ti oxides characterized by ring-shaped patterns with variable Nb content (Fig. 7f), involving variations of Nb concentration in the supergene fluids during laterite formation. Since Nb is leached through pyrochlore alteration (Fig. 13), such variations of Nb content result from variable rates of pyrochlore weathering associated with changes in paleoclimates leading to distinct weathering conditions.

The occurrence of rutile and brookite, as observed in the studied profile, is unusual in lateritic environments, and the specific conditions leading to their formation in supergene contexts remain elusive (Milnes and Fitzpatrick, 1989; Schulz et al., 2016). Due to lower surface energy, anatase is the first Ti oxide to crystallize (Navrotsky, 2003). In case of slow crystal growth, anatase can convert into nano-brookite under moderate acidic pH in the 3–6 range (Penn and Banfield, 1998; Zhang and Banfield, 2014; Schulz et al., 2016). Furthermore, the incorporation of minor elements in Ti oxides can influence phase transitions between the polymorphs (Hanaor and Sorrell, 2011). Minor concentrations of Fe^{3+} and V^{5+} favor the formation of brookite over anatase during Ti oxide precipitation (Khan and Berk, 2014). The formation of brookite in black shales from Meishucun has been assigned to the presence of V^{5+} during the crystallization of Ti oxides (Liu et al., 2019). The coprecipitation of Ti with Nb may have therefore promoted the formation of brookite, as it does for highly charged V^{5+}. Furthermore, the formation of rutile likely results from the brookite-to-rutile transition rather than the anatase-to-rutile phase transition as the presence of Nb^{5+} in anatase hinders its transition to rutile (Huberty and Xu, 2008) The brookite-to-rutile phase transition remains underexplored (Huberty et al., 2008) but the effect of temperature is excluded as the temperature of supergene processes remains low (Li and Ishigaki, 2004, Thorne et al., 2012).

The unusual presence of Nb in cerianite and hollandite indicates that a fraction of the Nb released by the alteration of primary Nb-bearing phases was mobilized in the vein with mobile elements such as Ba^{2+} and Mn^{2+}.The occurrence of Mn oxide minerals within the laterite appears to be a relatively late-stage phenomenon, as these minerals are found in fractures and cavities.

Hollandite may have formed due to alkaline conditions which lead to the oxidation of Mn^{2+} (Spier et al., 2006). When all Ba has been incorporated into hollandite, pyrolusite started to form. The precipitation of cerianite results from the oxidation of Ce^{3+} during the evaporation of the groundwater under positive Eh values and neutral to alkaline conditions (Braun et al., 1990; Akagi and Masuda, 1998; Janots et al., 2015). The presence of pyrolusite indicates that the manganiferous laterite reached the 0.5–1 V oxidation potential range and the pH range of 5–9 (Goldsmith et al., 2014). The co-occurrence of Mn and Ce oxides, which necessitate high oxidation potential and slightly alkaline conditions, may be influenced by the vicinity of the water table, which facilitates these conditions (Giovannini et al., 2017). The presence of minerals forming in slightly alkaline conditions suggests that Nb mobility may have resulted from the formation of polyoxometalate complexes which form under a pH of around 8 (Friis and Casey, 2018).

4.4 Mechanisms of incorporation and affinity for secondary phases

4.4.1 Iron oxides

Niobium K-edge XANES spectra indicate that Nb^{5+} substitutes for Fe^{3+} in goethite. The stability of Nb-bearing goethite unit cell parameters (Fig. S6) is expected considering the similar ionic radii of $^{VI}Fe^{3+}$ (0.645 Å) and $^{VI}Nb^{5+}$ (0.64 Å) (Shannon, 1976). Variations in the intensity of the pre-edge feature (18,992 eV) in the goethite spectrum (Fig. 11) suggest that the Nb site exhibits lower symmetry compared to the synthetic reference (Bollaert et al., 2023b) which may result from the incorporation of additional cations such as Ti^{4+} and Si^{4+} (Fig. 10a,b). The two trends of the evolution of Nb in function of Ti indicate distinct mechanisms of Nb^{5+} incorporation in Fe oxides. In the fragmented laterite, characterized by elevated bulk TiO_2 contents (3.4 wt%), the linear regression coefficient close to 1 between Nb and Ti (Fig. 10a) suggests mechanisms of substitution, possibly in the form of $2Fe^{3+} + 3H^{+} = Nb^{5+} + Ti^{4+}$ or $3Fe^{3+} = Nb^{5+} + Ti^{4+}$. In the lower purple laterite where Fe oxides have a Ti/Nb ratio of ca. 0.4, the lower presence of Ti^{4+} is compensated by the

incorporation of Si^{4+}. This compensation is evidenced by the correlation observed between Nb and Si, a correlation that is absent in the Fe oxides found in the fragmented horizon (see Fig. 10b).

Microchemical analyses indicate that goethite incorporates greater Nb amounts relative to hematite (Fig. 10b). This observation, coupled with the absence of a correlation between the relative abundance of hematite and its contribution to the average Nb speciation, indicates that hematite potential for Nb^{5+} is lower ithan goethite. Distinct crystal-chemical mechanisms of substitution account for this difference. The incorporation of Nb into goethite can be associated with the loss of H^+ ($Fe^{3+} + 2H^+ = Nb^{5+}$), as proposed for the incorporation of Sb^{5+} and U^{5+} into goethite (Bolanz et al., 2013; Kerisit et al., 2016). Through this process, the concentration of Nb in goethite is limited to 2.8 wt% Nb_2O_5, in agreement with the maximum concentrations measured (Fig. 10). Above this maximum concentration, excess of deprotonation would lead to the destabilization of goethite (Bolanz et al., 2013). In hematite, 3 Nb^{5+} can substitute for 5 Fe^{3+} but the amount of Nb^{5+} incorporated remains limited due to the formation of face-sharing Nb polyhedra inducing strong electrostatic repulsion unfavorable to the stability of the crystal structure (Bolanz et al., 2013).

The possibility of Nb sorption onto Fe oxides is ruled out by the shell-by-shell fit analysis of EXAFS data of the Nb-bearing goethite as the Nb local environment of the Nb-bearing goethite matches that of the reference compound (Fig. 12 and Table 4). Experimental evidence of Nb sorption onto goethite exists (Ghosh et al., 2017) but only at very low Nb concentrations (ca. 1.10 mol/L) which cannot lead to the Nb concentrations measured in Fe oxides (up to 2.8 wt%) in the studied profile.

4.4.2 Titanium oxides

The shifted diffraction peaks (Fig. S6) and the unit-cell parameters increase of Ti oxides are consistent with Nb incorporation into Ti oxides (Liu et al., 2016). The correlation between Fe + Ti and Nb concentrations (Fig. S5) suggests that the substitution of Nb^{5+} for Ti^{4+} is compensated by the incorporation of Fe^{3+} , following the substitution mechanism: $2Ti^{4+} = Nb^{5+} + Fe^{3+}$ (Giovannini et

al., 2017; Win et al., 2017). As for Fe oxides, Nb sorption onto Ti oxides is excluded due to the agreement between the site geometry of Nb in Ti oxides from the profile and their theoretical local structure in reference compounds (Table 4).

The similarity of Nb L_3-edge XANES and Nb K-edge EXAFS spectra of Nb-bearing rutile and brookite indicates similar Nb site geometry (Fig. 12). However, the expected local geometry of the Ti sites is different in rutile (D_{2h}) and in brookite (C_1) (Landmann et al., 2012). The similar spectral features between rutile and brookite may result from the inheritance of the Nb site geometry of brookite after its conversion into rutile. Local- and medium-range preservation of the Nb atomic environment is confirmed by the consistent fitting of the EXAFS spectra of rutile from the local structure of brookite (Fig. S8).

4.5 Implications for the conservative behavior of niobium

This study demonstrates that intense supergene weathering leads to the alteration of pyrochlore and Nb-bearing Ti oxides and to the release of Nb^{5+} into the supergene fluids. The capacity of rutile, brookite and goethite to incorporate Nb^{5+} limits Nb mobility in most horizons. However, the presence of Nb associated with mobile elements like Mn and Ce in the manganiferous vein indicates mobility at the scale of the lateritic profile, at least under slightly alkaline conditions in the zone of fluctuation of the water table.

The similarities between the Morro dos Seis Lagos laterite and findings regarding Nb mineralizations in a wide variety of laterites worldwide characterized by different protoliths and conditions of formation imply Nb mobilization during intense supergene weathering (Lottermoser and England, 1988; Wall et al., 1996; Chebotarev et al., 2017, Bollaert et al., 2023c). Nonetheless, studies often consider Nb as a chemical invariant in the critical zone based on geochemical data only (Kurtz et al., 2000; Holub et al., 2001; Berger et al., 2014; Chassé et al., 2019; Nabi et al., 2021, Guinoiseau et al., 2021; Braga and Biondi, 2023). Considering the potential Nb loss from the

studied system, future use of Nb as a geochemical invariant in mass-balance calculations should rely on a careful examination of the Nb hosts in the studied materials.

In this profile, Nb and other elements with limited mobility such as Th and Sc (Braun et al., 1993; Berger et al., 2014; Chassé et al., 2019) are mobilized, at least at the scale of the mineralogical assemblage. In the carbonatite, Th is hosted in pyrochlore, thorbastnaesite and monazite. Although the hosts for Sc are not identified by SEM due to low contents, the concomitant evolution along the profile of Th and Sc (Table S1) may indicate that they share the same phases in the laterite, i.e., neoformed cerianite, florencite as well as residual pyrochlore and monazite. This change of speciation may involve potential losses of Th and Sc during weathering. The progressive increase in Zr and Hf contents with decreasing depth indicates that they are little affected by alteration. Zircon has been identified as the main carrier of Zr and Hf which is often resistant to alteration (Colin et al., 1993). The absence of radionuclides in zircon limits metamictization, a factor favoring its alteration in other lateritic profiles (Balan et al., 2001). In this profile, Zr and Hf are the least mobile elements making them more suitable for use as conservative elements compared to Nb, Th, and Sc.

4.6 A new model of niobium enrichment in laterites

We highlight a new model accounting for the formation of Nb-enriched laterite, independent of the residual accumulation of pyrochlore as is the case in the Araxá and Catalão-I world-class Nb deposits (Palmieri et al., 2022; Braga and Biondi, 2023). The exceptional Nb concentration in the studied laterite (2.91 wt% Nb_2O_5 on average) results from the combination of the Nb enrichment of the siderite carbonatite inherited from late-carbo-magmatic-to-hydrothermal processes (Giovannini et al., 2020) and of Nb scavenging by secondary oxides during supergene processes. Despite unexpected intense alteration of pyrochlore, Nb concentration remains high in most of the profile due to its scavenging by secondary oxides, in particular goethite, brookite and rutile. This model of Nb enrichment depends on the capacity of Nb^{5+} to substitute for cations, released from the primary

Nb minerals, with secondary phases formed during the processes of alteration. Preservation of primary enrichment will thus depend on the chemistry of the parent rock, which must provide Fe and Ti for secondary oxides precipitation, and on the physico-chemical conditions of formation of the laterite, which must favor the precipitation of goethite and Ti oxides.

CONCLUSION

Niobium speciation was monitored along a hundred-meter-thick lateritic profile in the Morro dos Seis Lagos region. Hydrothermal Ba-Ce pyrochlore, Nb-bearing brookite, rutile and minor goethite host Nb in the siderite carbonatite parent rock. Textural and mineralogical evidence of pyrochlore and Nb-bearing Ti oxides alteration are corroborated spectroscopically by the decrease in their contribution to the average speciation of Nb all along the profile. Pyrochlore dissolution is almost complete in the top profile. The unusual alteration of pyrochlore results from the weakening of the octahedral framework due to the substitution of Fe^{3+} and Ti^{4+} for Nb^{5+}. The fate of Nb after its release from primary minerals depends on the mineralogy of the horizon. In the first stages of weathering, the abundance of Fe oxides results in Nb incorporation into goethite. The high concentration of Nb in goethite is explained by its crystal-chemistry, allowing Nb accommodation into its structure through chemical and structural modifications. Conversely, the capacity of hematite to incorporate Nb^{5+} is limited due to structural constraints. When precipitation of Ti oxides occurs in advanced stages of weathering, Nb^{5+} will preferentially incorporate brookite and rutile. Characteristic zoning with variable Nb concentrations reflects pulses of pyrochlore alteration and associated Nb leaching. The mechanisms of formation of brookite and rutile in a supergene environment, elusive so far, are constrained by spectroscopic results indicating the transformation of brookite into rutile. In the manganiferous vein, the presence of Nb in cerianite and hollandite demonstrates the mobility of Nb at the scale of the profile under slightly alkaline conditions resulting from the vicinity of the water table. This study demonstrates that residual accumulation of

pyrochlore is not necessary to observe Nb enrichment in weathering profiles. In the Morro dos Seis Lagos laterite, Nb accumulates in secondary phases after its leaching from pyrochlore due to the ability of Fe and Ti oxides to incorporate Nb^{5+}. The formation of these oxides is dependent on the geochemistry and mineralogy of the parent rock and of the physico-chemical conditions of weathering forming the profile. The mobilization of Nb in this profile questions the systematic use of Nb as a conservative element in lateritic contexts.

ACKNOWLEDGMENTS

We would like to express our sincere gratitude to Ludovic Delmes and Imène Estève from Sorbonne University for their assistance with XRD measurements and SEM analysis, respectively. We also extend our thanks to Andreï Lecomte and Olivier Rouer for their valuable support and efficiency during EPMA analysis. Our appreciation goes to Olivier Beyssac, Keevin Beneut and Anne Elisabeth Marceline for their assistance in Raman spectroscopy analysis. We acknowledge the provision of synchrotron radiation beamtime by SOLEIL on LUCIA (proposal No. 20200969) and CRISTAL (proposal No. 20211378, in the framework of CNRS RECIPROCS network) beamlines and the scientific support of E. Elkaïm. We are also grateful to ESRF synchrotron for providing beamtime on BM23 (Proposal No. ES-1036). Special thanks go to Cesare Atzori for his assistance in bulk XAS measurement. This work was conducted within the framework of the PhD thesis of Q. Bollaert at ED398 GRNE, Sorbonne University.

APPENDIX A: SUPPLEMENTARY MATERIAL

Research data will be uploaded on Zenodo repository (10.5281/zenodo.8398498). Supplementary material includes raw geochemical data and data analysis (Part 1), Raman spectra of Ti oxides (Part 2), EPMA analyses of Ti oxides (Part 3), diffraction patterns on bulk samples of Nb-bearing phases

(Part 4), simulation of experimental micro-XANES (Part 5) and additional shell-by-shell fits of Ti oxides spectra (Part 6).

References

Akagi T. and Masuda A. (1998) A simple thermodynamic interpretation of Ce anomaly. *Geochem. J.* **32**, 301–314.

Atencio D. (2021) Pyrochlore-Supergroup Minerals Nomenclature: An Update. *Front. Chem.* **9**, 713368.

Balan E., Neuville D. R., Trocellier P., Fritsch E., Muller J.-P. and Calas G. (2001) Metamictization and chemical durability of detrital zircon. *Am. Mineral.* **86**, 1025–1033.

Berger A., Janots E., Gnos E., Frei R. and Bernier F. (2014) Rare earth element mineralogy and geochemistry in a laterite profile from Madagascar. *Appl. Geochem.* **41**, 218–228.

Bevington Philip. R. and Robinson D. (1993) Data Reduction and Error Analysis for the Physical Sciences. *Comput. Phys.* **7**, 415–416.

Bolanz R. M., Bläss U., Ackermann S., Ciobotă V., Kolsch P., Tarcea N., Popp J. and Majzlan J. (2013) The Effect of Antimonate, Arsenate, and Phosphate on the Transformation of Ferrihydrite to Goethite, Hematite, Feroxyhyte, and Tripuhyite. *Clays Clay Miner.* **61**, 11–25.

Bollaert Q., Chassé M., Elnaggar H., Juhin A., Courtin A., Galoisy L., Quantin C., Retegan M., Vantelon D. and Calas G. (2023a) Niobium speciation in minerals revealed by $L_{2,3}$-edges XANES spectroscopy. *Am. Mineral.* **108**, 595–605.

Bollaert Q., Chassé M., Morin G., Baptiste B., Courtin A., Galoisy L., Landrot, G., Quantin C., Vantelon D. and Calas G. (2023b) Atomic-scale environment of niobium in minerals as revealed by X-ray absorption spectroscopy at the Nb K -edge. *Europ. J. Mineral.* Submitted.

Bollaert Q., Chassé M., Allard T., Courtin A., Galoisy L., Landrot, G., Quantin C., Vantelon D. and Calas G. (2023c) Multiscale processes controlling niobium mobility during supergene weathering. *Geochim. Cosmochim. Acta.* **353,** 142–157**.**

Braga J. M. and Biondi J. C. (2023) Geology, geochemistry, and mineralogy of saprolite and regolith ores with Nb, P, Ba, REEs (+ Fe) in mineral deposits from the Araxá alkali-carbonatitic complex, Minas Gerais state, Brazil. *J. South Am. Earth Sci.* **125**, 104311.

Braun J.-J., Pagel M., Herbilln A. and Rosin C. (1993) Mobilization and redistribution of REEs and thorium in a syenitic lateritic profile: A mass balance study. *Geochim. Cosmochim. Acta* **57**, 4419–4434.

Braun J.-J., Pagel M., Muller J.-P., Bilong P., Michard A. and Guillet B. (1990) Cerium anomalies in lateritic profiles. *Geochim. Cosmochim. Acta* **54**, 781–795.

Chassé M., Griffin W. L., O'Reilly S. Y. and Calas G. (2019) Australian laterites reveal mechanisms governing scandium dynamics in the critical zone. *Geochim. Cosmochim. Acta* **260**, 292–310.

Chakhmouradian, A. R., Reguir, E. P., Kressall, R. D., Crozier, J., Pisiak, L. K., Sidhu, R., and Yang, P. (2015). Carbonatite-hosted niobium deposit at Aley, northern British Columbia (Canada): Mineralogy, geochemistry and petrogenesis. *Ore Geol. Rev.* ***64***, 642-666.

Chebotarev D. A., Doroshkevich A. G., Klemd R. and Karmanov N. S. (2017) Evolution of Nb-mineralization in the Chuktukon carbonatite massif, Chadobets upland (Krasnoyarsk Territory, Russia). *Period. Mineral.* **86**.

Colin F., Alarçon C. and Vieillard P. (1993) Zircon: an immobile index in soils? *Chem. Geol.* **107**, 273–276.

Cordeiro P. F. de O., Brod J. A., Palmieri M., de Oliveira C. G., Barbosa E. S. R., Santos R. V., Gaspar J. C. and Assis L. C. (2011) The Catalão I niobium deposit, central Brazil: Resources, geology and pyrochlore chemistry. *Ore Geol. Rev.* **41**, 112–121.

Estrade G., Marquis E., Smith M., Goodenough K. and Nason P. (2019) REE concentration processes in ion adsorption deposits: Evidence from the Ambohimirahavavy alkaline complex in Madagascar. *Ore Geol. Rev.* **112**, 103027.

Friis H. and Casey W. H. (2018) Niobium Is Highly Mobile As a Polyoxometalate Ion During Natural Weathering. *Can. Mineral.* **56**, 905–912.

Geisler T., Berndt J., Meyer H.-W., Pollok K. and Putnis A. (2004) Low-temperature aqueous alteration of crystalline pyrochlore: correspondence between nature and experiment. *Mineral. Mag.* **68**, 905–922.

Ghosh, M., Swain, K.K., Verma, R., (2017). Interaction of niobium with iron-oxide colloids and the role of humic acid. *J. Environ. Radioact.* 178–179, 101–109.

Giovannini A. L., Bastos Neto A. C., Porto C. G., Pereira V. P., Takehara L., Barbanson L. and Bastos P. H. S. (2017) Mineralogy and geochemistry of laterites from the Morro dos Seis Lagos Nb (Ti, REE) deposit (Amazonas, Brazil). *Ore Geol. Rev.* **88**, 461–480.

Giovannini A. L., Bastos Neto A. C., Porto C. G., Takehara L., Pereira V. P. and Bidone M. H. (2021) REE mineralization (primary, supergene and sedimentary) associated to the Morro dos Seis Lagos Nb (REE, Ti) deposit (Amazonas, Brazil). *Ore Geol. Rev.* **137**, 104308.

Giovannini A. L., Mitchell R. H., Bastos Neto A. C., Moura C. A. V., Pereira V. P. and Porto C. G. (2020) Mineralogy and geochemistry of the Morro dos Seis Lagos siderite carbonatite, Amazonas, Brazil. *Lithos* **360–361**, 105433.

Goldsmith Y., Stein M. and Enzel Y. (2014) From dust to varnish: Geochemical constraints on rock varnish formation in the Negev Desert, Israel. *Geochim. Cosmochim. Acta* **126**, 97–111.

de Groot F. M. F., Hu Z. W., Lopez M. F., Kaindl G., Guillot F. and Tronc M. (1994) Differences between L_3 and L_2 x-ray absorption spectra of transition metal compounds. *J. Chem. Phys.* **101**, 6570–6576.

Guinoiseau D., Fekiacova Z., Allard T., Druhan J. L., Balan E. and Bouchez J. (2021) Tropical Weathering History Recorded in the Silicon Isotopes of Lateritic Weathering Profiles. *Geophys. Res. Lett.* **48**.

Hanaor D. A. H. and Sorrell C. C. (2011) Review of the anatase to rutile phase transformation. *J. Mater. Sci.* **46**, 855–874.

Holub S.M., Spears J. D. H. and Lajtha K. (2001) A reanalysis of nutrient dynamics in coniferous coarse woody debris. *Can. J. For. Res.* **31,** 1894–1902.

Huberty J. and Xu H. (2008) Kinetics study on phase transformation from titania polymorph brookite to rutile. *J. Solid State Chem.* **181**, 508–514.

Issler R. S. and Silva G. G. (1980) The seis Lagos carbonatite complex. In Congresso Brasileiro de Geologia. Cambori\'u, Santa Catarina. pp. 1564–1572.

Janots E., Bernier F., Brunet F., Muñoz M., Trcera N., Berger A. and Lanson M. (2015) Ce(III) and Ce(IV) (re)distribution and fractionation in a laterite profile from Madagascar: Insights from in situ XANES spectroscopy at the Ce L_{III}-edge. *Geochim. Cosmochim. Acta* **153**, 134–148.

Kerisit S., Bylaska E. J., Massey M. S., McBriarty M. E. and Ilton E. S. (2016) Ab Initio Molecular Dynamics of Uranium Incorporated in Goethite (α-FeOOH): Interpretation of X-ray Absorption Spectroscopy of Trace Polyvalent Metals. *Inorg. Chem.* **55**, 11736–11746.

Khan A., Faisal S., Ullah Z., Ali L., Ghaffari A., Nawab J. and Rashid M. U. (2021) Pyrochlore-group minerals from the Loe-Shilman Carbonatite Complex, NW Pakistan: implications for evolution of carbonatite system. *Period. Mineral.* **90**(2), 277-287.

Khan H. and Berk D. (2014) Synthesis, physicochemical properties and visible light photocatalytic studies of molybdenum, iron and vanadium doped titanium dioxide. *React. Kinet. Mech. Catal.* **111**, 393–414.

Kurtz A. C., Derry L. A., Chadwick O. A. and Alfano M. J. (2000) Refractory element mobility in volcanic soils. *Geology* **28**, 683–686.

Landmann M., Rauls E. and Schmidt W. G. (2012) The electronic structure and optical response of rutile, anatase and brookite TiO_2. *J. Phys. Condens. Matter* **24**, 195503.

Li T., Li Z., Fan G., Fan H., Zhong J., Jahdali N. S., Qin M., Jehani A. M., Wang F. and Nahdi M. M. (2020) Hydroxyplumbopyrochlore, $(Pb_{1.5},\square_{0.5})Nb_2O_6(OH)$, a new member of the pyrochlore group from Jabal Sayid, Saudi Arabia. *Mineral. Mag.* **84**, 785–790.

Li J.-G. and Ishigaki T. (2004) Brookite → rutile phase transformation of TiO_2 studied with monodispersed particles. *Acta Mat.*, **52**, 5143-5150.

Liu G., Fan H., Xu J., Liu Z. and Zhao Y. (2016) Colossal permittivity and impedance analysis of niobium and aluminum co-doped TiO_2 ceramics. *RSC Adv.* **6**, 48708.

Liu Z.-R. R., Zhou M.-F., Williams-Jones A. E., Wang W. and Gao J.-F. (2019) Diagenetic mobilization of Ti and formation of brookite/anatase in early Cambrian black shales, South China. *Chem. Geol.* **506**, 79–96.

Lottermoser B. G. (1990) Rare-earth element mineralisation within the Mr. Weld carbonatite laterite, Western Australia. *Lithos* **24**, 151–196.

Lottermoser B. G. and England B. M. (1988) Compositional variation in pyrochlores from the Mt Weld carbonatite laterite, Western Australia. *Mineral. Petrol.* **38**, 37–51.

Lumpkin G. R., Ewing R. C., Williams C. T. and Mariano A. N. (2000) An Overview of the Crystal Chemistry, Durability, and Radiation Damage Effects of Natural Pyrochlore. *MRS Proc.* **663**, 921.

Mathé, P. E., Rochette, P., Vandamme, D., and Colin, F. (1999). Volumetric changes in weathered profiles: iso-element mass balance method questioned by magnetic fabric. *Earth Planet. Sci. Lett.* ***167***(3-4), 255-267.

Mathon O., Beteva A., Borrel J., Bugnazet D., Gatla S., Hino R., Kantor I., Mairs T., Munoz M., Pasternak S., Perrin F. and Pascarelli S. (2015) The time-resolved and extreme conditions XAS (TEXAS) facility at the European Synchrotron Radiation Facility: the general-purpose EXAFS bending-magnet beamline BM23. *J. Synchrotron Radiat.* **22**, 1548–1554.

Meagher E. P. and Lager G. A. (1979) Polyhedral thermal expansion in the TiO_2 polymorphs; refinement of the crystal structures of rutile and brookite at high temperature. *Can. Mineral.* **17**, 77–85.

Melgarejo J. C., Costanzo A., Bambi A. C. J. M., Gonçalves A. O. and Neto A. B. (2012) Subsolidus processes as a key factor on the distribution of Nb species in plutonic carbonatites: The Tchivira case, Angola. *Lithos* **152**, 187–201.

Milnes A. R. and Fitzpatrick R. W. (1989) Titanium and Zirconium Minerals. In *Minerals in Soils Environments (2nd edition)* (eds. J. B. Dixon and S. B. Weed). pp. 1031–1206.

Mitchell R. H. (2015) Primary and secondary niobium mineral deposits associated with carbonatites. *Ore Geol. Rev.* **64**, 626–641.

Miyawaki R., Momma K., Matsubara S., Sano T., Shigeoka M. and Horiuchi H. (2021) Hydroxykenopyrochlore, $(\square,Ce,Ba)_2(Nb,Ti)_2O_6(OH,F)$, a new member of the pyrochlore group from Araxá, Minas Gerais, Brazil. *Can. Mineral.* **59**, 589–601.

Nahon D. and Merino E. (1986) Pseudomorphic replacement versus dilation in laterites: petrographic evidence, mechanisms, and consequences for modelling. *J. Geochem. Explor.* **57**, 217–225.

Nasraoui M. and Bilal E. (2000) Pyrochlores from the Lueshe carbonatite complex (Democratic Republic of Congo): a geochemical record of different alteration stages. *J. Asian Earth Sci.* **18**, 237–251.

Nasraoui M., Bilal E. and Gibert R. (1999) Fresh and weathered pyrochlore studies by Fourier transform infrared spectroscopy coupled with thermal analysis. *Mineral. Mag.* **63**, 567–578.

Navrotsky A. (2003) Energetics of nanoparticle oxides: interplay between surface energy and polymorphism. *Geochem. Trans.* **4**, 34.

Newville M. (2013) Larch: An Analysis Package for XAFS and Related Spectroscopies. *J. Phys. Conf. Ser.* **430**, 012007.

Newville M. and Ravel B. (2020) *IFEFFIT* and *LARCH*. In *X-ray absorption spectroscopy and related techniques* (eds. C. T. Chantler, F. Boscherini, and B. Bunker,). International Tables for Crystallography.

Palmieri M., Brod J. A., Cordeiro P., Gaspar J. C., Barbosa P. A. R., de Assis L. C., Junqueira-Brod T. C., Silva S. E. e, Milanezi B. P., Machado S. A. and Jácomo M. H. (2022) The Carbonatite-Related Morro do Padre Niobium Deposit, Catalão II Complex, Central Brazil. *Econ. Geol.* **117**, 1497–1520.

Peiffert, C., Nguyen-Trung, C., Palmer, D. A., Laval, J. P., and Giffaut, E. (2010). Solubility of B-Nb_2O_5 and the hydrolysis of niobium (V) in aqueous solution as a function of temperature and ionic strength. *J. Solut. Chem.* ***39***, 197-218.

Penn R. L. and Banfield J. F. (1998) Oriented attachment and growth, twinning, polytypism, and formation of metastable phases; insights from nanocrystalline TiO_2. *Am. Mineral.* **83**, 1077–1082.

Ribeiro da Costa I., Roseiro J., Figueiras J., Rodrigues P. C. R. and Mateus A. (2021) Pyrochlore from the Bailundo Carbonatite Complex (Angola): Compositional variation and implications to mineral exploration. *J. Afr. Earth Sci.* **177**, 104154.

Rocha, E., Nasraoui, M., Soubiès, F., Bilal, E., and de Parseval, P. (2001). Évolution géochimique du pyrochlore au cours de l'altération météorique du gisement de Catalão II (Goiás, Brésil). *Comptes Rendus de l'Académie des Sciences-Series II A-Earth and Planetary Science*, ***332***(2), 91-98.

Rodríguez-Carvajal J. (1993) Recent advances in magnetic structure determination by neutron powder diffraction. *Phys. B Condens. Matter*, 55–69.

Rossoni M. B., Bastos Neto A. C., Souza V. S., Marques J. C., Dantas E., Botelho N. F., Giovannini A. L. and Pereira V. P. (2017) U-Pb zircon geochronologycal investigation on the Morro dos Seis Lagos Carbonatite Complex and associated Nb deposit (Amazonas, Brazil). *J. South Am. Earth Sci.* **80**, 1–17.

Schulz H.-M., Wirth R. and Schreiber A. (2016) Nano-Crystal Formation of Tio $_2$ Polymorphs Brookite and Anatase Due To Organic—Inorganic Rock–Fluid Interactions. *J. Sediment. Res.* **86**, 59–72.

Schwertmann U. (1971) Transformation of hematite to goethite in soils. *Nature* **232**, 624–625.

Shannon R. D. (1976) Revised effective ionic radii and systematic studies of interatomic distances in halides and chalcogenides. *Acta Crystallogr.* **A32**, 751–767.

Spier C. A., Vasconcelos P. M. and Oliviera S. M. B. (2006) $^{40}Ar/^{39}Ar$ geochronological constraints on the evolution of lateritic iron deposits in the Quadrilátero Ferrífero, Minas Gerais, Brazil. *Chem. Geol.* **234**, 79–104.

Stern E. A. (1993) Number of relevant independent points in x-ray-absorption fine-structure spectra. Phys. Rev. B. **48**(13), 9825–9827.

Tardy Y. and Nahon D. (1985) Geochemistry of laterites, stability of Al-goethite, Al-hematite, and Fe^{3+}-kaolinite in bauxites and ferricretes; an approach to the mechanism of concretion formation. *Am. J. Sci.* **285**, 865–903.

Thorne, R. L., Roberts, S., and Herrington, R. (2012). Climate change and the formation of nickel laterite deposits. *Geology*, ***40***(4), 331-334.

Vantelon D., Trcera N., Roy D., Moreno T., Mailly D., Guilet S., Metchalkov E., Delmotte F., Lassalle B., Lagarde P. and Flank A.-M. (2016) The LUCIA beamline at SOLEIL. *J. Synchrotron Radiat.* **23**, 635–640.

Vasconcelos M., Renne P. R., Brimhall G. H. and Becker T. A. (1994) Direct dating of weathering phenomena by $^{40}Ar/^{39}Ar$ and K-Ar analysis of supergene K-Mn oxides. *Geochim. Cosmochim. Acta* **58**, 1635–1665.

Viegas Filho J. R. and Bonow C. W. (1976) *Projeto Seis Lagos (Internal Report)*. Companhia de Pesquisa de Recursos Minerais, Manaus.

Wall F., Williams C. T., Woolley A. R. and Nasraoui M. (1996) Pyrochlore from Weathered Carbonatite at Lueshe, Zaire. *Mineral. Mag.* **60**, 731–750.

Williams, C. T., Wall, F., Woolley, A. R., and Phillips, S. (1997). Compositional variation in pyrochlore from the Bingo carbonatite, Zaire. *J. Afr. Earth Sci*, ***25***(1), 137-145.

Williams-Jones A. E. and Vasyukova O. V. (2022) Niobium, Critical Metal, and Progeny of the Mantle. *Econ. Geol. **18**(4), 837-855*

Win M. M., Enami M., Kato T. and Thu Y. K. (2017) A mechanism for Nb incorporation in rutile and application of Zr-in-rutile thermometry: A case study from granulite facies paragneisses of the Mogok metamorphic belt, Myanmar. *Mineral. Mag.* **81**, 1503–1521.

Wu B., Hu Y.-Q., Bonnetti C., Xu C., Wang R.-C., Zhang Z.-S., Li Z.-Y. and Yin R. (2021) Hydrothermal alteration of pyrochlore group minerals from the Miaoya carbonatite complex, central China and its implications for Nb mineralization. *Ore Geol. Rev.* **132**, 104059.

Wu Z., Chen Y., Wang Y., Xu Y., Lin Z., Liang X. and Cheng H. (2023) Review of rare earth element (REE) adsorption on and desorption from clay minerals: Application to formation and mining of ion-adsorption REE deposits. *Ore Geol. Rev.* **157**, 105446.

Zhang H. and Banfield J. F. (2014) Structural Characteristics and Mechanical and Thermodynamic Properties of Nanocrystalline TiO_2. *Chem. Rev.* **114**, 9613–9644.

wt%	Carb.8	Carb.12	Brown.2	Brown.10	Purple.2	Purple.11	Fragmented.9	Fragmented.5
A-site								
BaO	9.06	11.9	0.45	< d.l.	1.16	0.13	0.11	0.1
CaO	0.23	0.07	0.08	0.06	0	0.08	0.26	0.05
Ce_2O_3	9.9	9.79	14.82	14.17	11.46	12.59	8.7	3.45
K_2O	0.07	0.15	0.15	0.06	0.05	0.33	0.35	0.01
La_2O_3	1.86	1.8	0.38	0.56	2.92	1.86	1.95	1.98
Na_2O	1.63	0.85	0.56	0.16	0.03	0.1	0.29	0.12
Nd_2O_3	1.9	1.44	0.2	0.47	1.44	0.94	0.75	0.17
PbO	1.38	1.8	21.39	25.79	8.14	16.69	16.95	30.65
Sm_2O_3	0.36	0.16	< d.l.	< d.l.	0.08	< d.l.	0.13	< d.l.
SrO	0.33	0.19	0.05	< d.l.	< d.l.	< d.l.	< d.l.	0.03
ThO_2	0.33	0.19	0.05	< d.l.	< d.l.	5.16	4.23	4.19
Y_2O_3	0.16	0.17	0.13	0.03	1.41	[illegible]	0.09	0.05
B-site								
Al_2O_3	0.17	0.19	< d.l.	< d.l.	0.07	0.11	0.14	< d.l.
Fe_2O_3	5.14	3.83	3.04	4.6	3.48	4.46	7.33	3.91
Nb_2O_5	54.53	59.61	55.66	54.48	52.91	42.16	48.62	49.52
TiO_2	4.59	3.09	0.75	0.48	0.23	3.55	7.02	0.01
SiO_2	4.0	2.19	0.02	0.11	0.17	0.6	1.65	2.18
Total	96.6	97.49	100.73	101.91	95.12	88.88	98.69	96.54
Normalization to 2 B-site cations								
A-site								
Ba	0.194	0.267	0.012	0.000	0.029	0.004	0.002	0.003
Ca	0.013	0.004	0.026	0.004	0.000	0.007	0.016	0.004
Ce	0.189	0.196	0.386	0.342	0.252	0.336	0.173	0.087
K	0.005	0.011	0.014	0.005	0.004	0.032	0.025	0.001
La	0.037	0.036	0.010	0.014	0.068	0.052	0.041	0.052
Na	0.173	0.094	0.077	0.021	0.004	0.015	0.032	0.017
Nd	0.037	0.029	0.005	0.012	0.032	0.026	0.015	0.004
Pb	0.020	0.028	0.407	0.480	0.138	0.343	0.259	0.593
Sm	0.007	0.003	0.000	0.000	0.002	0.000	0.003	0.000
Sr	0.010	0.006	0.002	0.000	0.000	0.000	0.000	0.001
Th	0.004	0.002	0.001	0.000	0.000	0.090	0.055	0.068
Y	0.005	0.005	0.005	0.001	0.047	0.000	0.003	0.002
Total A-site	0.695	0.685	0.904	0.879	0.582	0.901	0.623	0.831
B-site								
Al	0.011	0.013	0.000	0.000	0.005	0.010	0.009	0.000
Fe	0.235	0.184	0.180	0.266	0.183	0.285	0.348	0.235
Nb	1.347	1.545	1.779	1.702	1.506	1.456	1.249	1.608
Ti	0.189	0.133	0.040	0.025	0.295	0.204	0.300	0.001
Si	0.219	0.126	0.001	0.008	0.011	0.046	0.094	0.157

wt%	Carb.1	Carb.13	Purple.27	Purple.25	Fragmented.
Al_2O_3	< l.d.	0.10	0.02	0.06	0.59
Fe_2O_3	12.36	8.31	12.23	11.86	13.25
K_2O	9.21	0.49	0.34	0.49	0.38
MnO	0.10	0.06	< l.d.	< l.d.	< l.d.
Nb_2O_5	2.20	12.43	15.62	16.80	20.12
P_2O_5	0.09	0.43	0.21	0.25	0.41
SiO_2	0.17	0.04	0.66	0.89	0.64
TiO_2	77.65	77.62	70.59	68.97	65.38
WO_3	< l.d.	1.78	0.37	< l.d.	0.37
Total	101.6	101.26	100.33	98.62	101.13
Normalization to 2 oxygens					
Al	0.000	0.002	0.000	0.001	0.010
Fe	0.124	0.088	0.132	0.130	0.143
K	0.164	0.009	0.006	0.009	0.007
Mn	0.000	0.001	0.000	0.000	0.000
Nb	0.019	0.079	0.101	0.106	0.131
P	0.000	0.003	0.001	0.002	0.002
Si	0.000	0.001	0.009	0.013	0.009
Ti	0.838	0.821	0.760	0.753	0.706
W	0.003	0.007	0.003	0.000	0.001

wt%	Carb.16	Lower Purple.157	Man-gan.15	Man-gan.44	Upper Pur-	Upper Pur-	Fragment-ed.95
Al_2O_3	1.44	0.35	1.39	0.53	0.20	1.32	1.59
Fe_2O_3	85.85	84.57	83.53	83.17	88.20	97.09	84.5
K_2O	<l.d.	<l.d.	0.01	<l.d.	<l.d.	0.02	<l.d.
MnO	0.03	0.47	0.22	0.53	0.37	<l.d.	<l.d.
Nb_2O_5	0.50	0.99	<l.d.	0.17	0.16	0.27	0.57
P_2O_5	0.15	<l.d.	<l.d.	0.00	< l.d.	0.24	1.25
SiO_2	0.18	0.61	1.53	0.68	0.07	0.15	<l.d.
TiO_2	0.13	0.25	0.02	< l.d	< l.d.	< l.d.	0.33
WO_3	< l.d.	< l.d.	0.21	< l.d.	< l.d.	< l.d.	0.05
Total	88.27	88.11	86.92	85.10	89.00	99.08	88.31
Normalization							
Al	0.051	0.012	0.049	0.019	0.007	0.041	0.056
Fe	1.924	1.925	1.883	1.939	1.980	1.943	1.895
K	0.000	0.000	0.000	0.000	0.000	0.001	0.000
Mn	0.001	0.012	0.006	0.014	0.009	0.000	0.000
Nb	0.007	0.014	0.000	0.002	0.002	0.003	0.008
P	0.002	0.000	0.000	0.000	0.000	0.003	0.016
Si	0.005	0.018	0.046	0.021	0.002	0.004	0.000
Ti	0.003	0.006	0.000	0.000	0.000	0.000	0.007
W	0.000	0.000	0.002	0.000	0.000	0.000	0.000

Sample	R_{calc} (Å)	R_{ref} (Å) pure	N	σ (Å²)	ΔE_0 (eV)	χ^2_R
Nb rutile	1.95 (± 0.009)	1.947–1.982	6.0 Nb–O	0.008 (± 0.0006)	-5.70 (± 0.7)	1.59
	3.02 (± 0.015)	2.96	2.0 Nb–Ti	0.003 (± 0.001)	–	
	3.39 (± 0.015)	3.57	8.0 Nb–Nb	0.012(± 0.001)	–	
Nb brookite	1.95 (± 0.02)	1.86–2.05	6.0 Nb–O	0.012 (± 0.001)	-8.57 (± 1.7)	2.74
	2.82 (± 0.10)	2.95	3.0 Nb–Nb	0.014 (± 0.002)	–	
	3.57 (± 0.05)	3.52	4.0 Nb–Ti	0.009 (± 0.002)	–	
Nb goethite	1.95 (± 0.05)	1.93–2.11	6.0 Nb–O	0.017 (± 0.0009)	-7.27 (± 0.7)	1.52
	3.09 (± 0.07)	3.02	3.0 Nb–Fe	0.011 (± 0.0004)	–	
	3.61 (± 0.16)	3.45	3.0 Nb–Fe	0.016 (± 0.0012)	–	

Declaration of interests

☒The authors declare that they have no known competing financial interests or personal relationships that could have appeared to influence the work reported in this paper.

☐The authors declare the following financial interests/personal relationships which may be considered as potential competing interests: